# Development of a Tunable and Compact Source of Squeezed States of Light

Dissertation
zur Erlangung des Doktorgrades
an der Fakultät für Mathematik, Informatik und Naturwissenschaften
Fachbereich Physik
der Universität Hamburg

vorgelegt von
Malte Hagemann

Hamburg
2024

| | |
|---|---|
| Gutachter/innen der Dissertation: | Prof. Dr. Ralf Riedinger |
| | Prof. Dr. Roman Schnabel |
| Zusammensetzung der Prüfungskommission: | Prof. Dr. Oliver Gerberding |
| | Prof. Dr. Ludwig Mathey |
| | Prof. Dr. Henning Moritz |
| | Prof. Dr. Ralf Riedinger |
| | Prof. Dr. Roman Schnabel |
| Vorsitzende/r der Prüfungskomission: | Prof. Dr. Ludwig Mathey |
| Datum der Disputation: | 07.06.2024 |
| Vorsitzender Fach-Promotionsausschusses PHYSIK: | Prof. Dr. Markus Drescher |
| Leiter des Fachbereichs PHYSIK: | Prof. Dr. Wolfgang J. Parak |
| Dekan der Fakultät MIN: | Prof. Dr.-Ing. Norbert Ritter |

# Abstract

Squeezed states of light are a commonly used quantum resource in the fields of quantum optics and quantum sensing. Nevertheless, sources of squeezed states of light still need to be further developed to open up more widespread application possibilities. This thesis investigated two different cavity designs for the generation of squeezed vacuum states based on cavity-enhanced parametric down-conversion. The objective was to provide a compact source with a stable generation of high squeeze factors at a wavelength of 1550 nm, allowing for flexible implementation in subsequent experiments.

In a setup utilizing doubly-resonant monolithic cavities, which consisted of bi-convex and coated ppKTP crystals, a squeeze factor of $(10.4 \pm 0.1)$ dB was achieved. The experiment focussed on adjusting the double resonance condition of monolithic resonators via a multi-temperature heating scheme. In order to ensure transportability, the experiment was conducted on a 80 cm x 80 cm breadboard.

A second experiment focussed on a half-monolithic design comprising a plano-convex ppKTP crystal and one mirror, and was set up on a more compact 40 cm x 60 cm breadboard. The generated squeeze factors were $>(10.5 \pm 0.1)$ dB and tunable over a wavelength range from 1549.9 nm to 1550.34 nm with a maximum at $(11.0 \pm 0.1)$ dB. The coherent control locking scheme ensured a stable squeezed phase over a period of 8 hours. Thus, the presented setup meets the requirements for a flexible application in experiments conducted within the telecommunication wavelength range.

In addition, a mirror surface characterization design based on a Mach- Zehnder interferometer was engineered. With a lateral resolution of $(5.29 \pm 0.06)\,\mu\mathrm{m}$ and a sensitivity of $(3.1 \pm 1.4)\,\mathrm{fm}/\sqrt{\mathrm{Hz}}$, the interferometer could scan an $56\,\mathrm{mm}^2$ circular excerpt of the mirror within 200 seconds. A digital reconstruction enabled mapping of the mirror's surface roughness and optical loss. This method visualised point absorbers in the coating, which could cause thermal distortions in experiments with high-power laser light. The interferometer was shot-noise limited for frequencies beyond 85 kHz. Implementing squeezed states of light could enhance the sensitivity beyond the quantum limit in the signal range, once the noise is reduced to the shot-noise limit for frequencies below 65 kHz.

# Kurzfassung

Gequetschte Lichtzustände sind eine häufig genutzte Quantenressource in den Bereichen Quantenoptik und -sensorik. Dennoch müssen Quellen für gequetschte Lichtzustände weiter entwickelt werden, um breitere Anwendungsmöglichkeiten zu eröffnen. In dieser Arbeit wurden zwei verschiedene Kavitätdesigns für die Erzeugung von gequetschten Vakuumzuständen basierend auf der kavitätsverstärkten parametrischen Abwärtskonversion untersucht. Ziel war es, eine kompakte Quelle mit einer stabilen Erzeugung von hohen Quetschzuständen bei einer Wellenlänge von 1550 nm zu schaffen, die eine flexible Implementierung in nachfolgenden Experimenten ermöglicht.

In einem Aufbau mit doppelresonanten monolithischer Kavitäten, die aus bikonvexen und beschichteten ppKTP-Kristallen bestanden, wurde ein Quetschfaktor von $(10,4 \pm 0,1)$ dB erreicht. Das Experiment konzentrierte sich auf die Einstellung der Doppelresonanzbedingung von monolithischen Resonatoren durch ein Multi-Temperatur-Heizschema. Um die Transportfähigkeit zu gewährleisten, wurde das Experiment auf einer 80 cm x 80 cm Lochrasterplatte durchgeführt.

Ein zweites Experiment konzentrierte sich auf ein halb-monolithisches Design, das ein plankonvexen ppKTP-Kristall und ein Spiegel umfasste, und wurde auf einer kompakteren 40 cm x 60 cm Lochrasterplatine aufgebaut. Die erzeugten Quetschfaktoren waren $>(10,5 \pm 0,1)$ dB und einstellbar über einen Wellenlängenbereich von 1549,9 nm bis 1550,34 nm mit einem Maximum bei $(11,0 \pm 0,1)$ dB. Die „Coherent Control“ Regelschleife gewährleistete eine stabile Quetschphase über einen Zeitraum von 8 Stunden. Damit erfüllt der vorgestellte Aufbau die Anforderungen für einen flexiblen Einsatz bei Experimenten im Telekommunikationswellenlängenbereich.

Darüber hinaus wurde ein Design zur Charakterisierung der Spiegeloberfläche auf der Grundlage eines Mach-Zehnder-Interferometers entwickelt. Mit einer lateralen Auflösung von $(5,29 \pm 0,06)$ µm und einer Empfindlichkeit von $(3,1 \pm 1,4)\,\mathrm{fm}/\sqrt{\mathrm{Hz}}$ konnte das Interferometer einen $56\,\mathrm{mm}^2$ zirkularen Ausschnitt des Spiegels innerhalb von 200 Sekunden scannen. Eine digitale Rekonstruktion ermöglichte die Abbildung der Oberflächenrauhigkeit und des optischen Verlusts des Spiegels. Mit dieser Methode wurden Punktabsorber in der Beschichtung sichtbar gemacht, die bei Experimenten mit Hochleistungslaserlicht thermische Verzerrungen verursachen können. Das Interferometer war bei Frequenzen über 85 kHz durch das Schrotrauschen limitiert. Die Implementierung von gequetschten Lichtzuständen könnte die Empfindlichkeit über das Quantenlimit im Signal bereich hinaus verbessern, sobald das Rauschen auf das Schrotrauschlimit für Frequenzen unter 65 kHz reduziert ist.

# Contents

# Chapter 1

# Introduction

The Heisenberg uncertainty principle forms a fundamental property of quantum mechanics. It states that two non-commuting observables, for instance the position and momentum of electrons, cannot be measured with an arbitrary precision at the same time [Hei27]. In the quantum mechanical description of light, the amplitude and phase of a light wave form such a pair of non-commuting observables. Even for minimal uncertainty, coherent light sources, such as carefully designed lasers, exhibit amplitude and phase fluctuations resulting in what is known as quantum noise upon detection. Quantum noise can also be measured for light in the ground state, which contains no photons at all and results from vacuum fluctuations in the harmonic oscillator description, using a balanced homodyne detection scheme. However in the case of squeezed states of light, the uncertainty of one observable is below (= squeezed) the ground state uncertainty, resulting in a lower quantum noise compared to the coherent state for that observable. That comes at the cost of an increased uncertainty in the orthogonal observable (= anti-squeezed).

It took decades after the first appearances of squeezed states of light in theoretical works to observe them experimentally in 1985 by Slusher et al [AGML16] [SHY+85]. They used sodium atoms as a non-linear medium to create a squeezed state of light by four wave mixing and observed a noise reduction of 0.3 dB. To improve the generation of squeezed light, cavities for the pump and squeezed field were utilized. Already in 1986 a squeeze factor of 3 dB was observed by using the parametric down-conversion process [WKHW86]. Here, a MgO:LiNbO$_3$ crystal functioned as the non linear medium to create the squeezed states of light at a wavelength of 1.06 µm. Further developing and improving the technique of cavity-enhanced parametric down-conversion paved the way to observe a squeeze factor of 10 dB in 2008 [VMC+08]. The current record squeeze factor of 15 dB was observed in 2016 [VMDS16]. Both observations beyond the 10 dB mark were generated at a wavelength of 1064 nm. Beside the work on increasing the squeeze factors, squeezed states of light have been realized in optical [BGS$^+$15] [HGP$^+$06] and further infrared wavelengths [DFGSS21] [MWV22], and observed at frequency regions ranging from a few Hz [VKL$^+$10] [MAE$^+$11] to GHz [AMS13] and THz [KTY$^+$20]. Tunable squeezed states of light sources have also been a research aspect and were realized in the optical wavelength region [PCK92] [BRF97] [KCL21] with a tuning bandwidth of up to 10 nm [FWS$^+$93]. However, these tunable sources suffered from low squeezing factors of 5 dB [PCK92] or even less than 2 dB [BRF97] [KCL21] [FWS$^+$93].

Simultaneous to the research on squeezed state of light sources, the field of applications widened. Some examples are the enhanced sensitivity in biological measurements [TJD$^+$13], calibration of photo sensors without a standard candle [VMDS16], one-sided device independent quantum key distributions [GHD$^+$15], and spectroscopy in the case of tunable sources [PCK92]. Yet the most prominent application of squeezed states of light is the sensitivity enhancement by decreasing the shot noise limit of interferometers, especially in gravitational wave detectors [Sch17]. GEO600 was the first detector to be equipped with this technology in 2011 [A$^+$11] [GDD$^+$13], followed by VIRGO and LIGO, which improved the sensitivities beyond the quantum limit [AAA$^+$19] [TYK$^+$19]. Alternatively, the laser power can be increased to enhance the sensitivity in the shot noise limited region [Sch17]. However, it is important to note that the laser power is limited due to potential thermal lensing in the beam splitter and arm cavities [WDRS91], as well as an increased coating thermal noise resulting from heating the coatings and substrates of the test masses [B$^+$14]. Therefore, it is crucial to carefully consider the laser power used in order to avoid these issues. Recent findings from 2021 have further highlighted the impact of high laser power on the test masses, where point absorbers enclosed during the coating process exacerbate this effect even further and ultimately lead to distortions in surface [BVY$^+$21]. These distortion can contribute to scattered light decreasing the overall sensitivity.

Usually, the squeezed state of light sources in before-mentioned experiments were set up on large optical tables. However, a requirement for more widespread use of the technology is the development of a transportable and compact setup. The GEO600 source was the first transportable device designed with a footprint of 1.35 m x 1.35 m [KVL$^+$12]. In 2018, a 1550 nm squeezed state of light source was engineered with a further decreased footprint of 80 cm x 80 cm [Sch18]. However, this design is still relatively large compared to typical table-top laser systems.

Hence, the primary objective of this thesis was to conduct further research on the generation of squeezed states of light, with the aim of creating a more compact and tuneable source. The focus was on investigating the generation through doubly resonant cavity-enhanced parametric down-conversion. Two cavity designs were compared, namely the monolithic and half-monolithic (known as hemilithic) cavity, at a wavelength of 1550 nm. The chosen wavelength enables the application in the telecommunications sector, since it is one of the communication wavelengths. Considering plans for some future gravitational wave detectors like the Einstein Telescope to be operated at 1550 nm light [Tea20], this wavelength is even more interesting for the research on squeezed states of light.

The second goal of this thesis was the development of a Mach-Zehnder interferometer for characterizing mirror surfaces. The focus laid on the determination of point absorbers, surface roughness and reflectivity. The design choice of a Mach-Zehnder interferometer allows for the application of squeezed light in general.

This thesis is structured as follows:

- Chapter 2 presents the theoretical foundations to describe squeezed states of light. Here, an introduction to the quantization of light and non linear optics are given to understand the parametric down-conversion process used to generate squeezed states of light.
- Chapter 3 describes the generation of squeezed vacuum states at 1550 nm utilizing monolithic cavities and investigates the requirements for double resonance inside the cavities.
- Chapter 4 presents a compact squeezed vacuum source based on a hemilithic cavity design tunable over roughly 0.5 nm around the center wavelength of 1550 nm.
- Chapter 5 demonstrates the concept to characterize mirror surfaces for roughness, point absorbers, and reflectivity based on a Mach-Zehnder interferometer.
- Chapter 6 summarizes and discusses the previous mentioned results of this thesis.

# Chapter 2

# Theory of squeezed states of light

## 2.1 Quantum-mechanical description of light

To describe phenomena like squeezed states of light or entanglement, a quantum mechanical description of light is required, since the classical approach is not sufficient. The given description in this chapter is primarily based on the textbook *Introductory Quantum Optics* by C.C. Gerry and P.L. Knight [GK05] and the lecture *Einführung in die theoretischen Grundlagen der Quanten- und Atomphysik* held by Prof. Dr. Schmelcher.

### 2.1.1 Quantization of the electromagnetic field

Assuming a cavity with length $L$ and perfectly conductive walls at $z = 0$ and $z = L$, then the electromagnetic single mode field is given by $\vec{E} = (E_x, 0, 0)$ and $\vec{B} = (0, B_y, 0)$ and propagates along the $z$ direction. The components $E_x$ and $B_y$ are given by

$$E_x = \sqrt{\frac{2\nu^2}{V\epsilon_0}} q(t) \sin(kz), \tag{2.1}$$

$$B_y = (\frac{\mu_0\epsilon_0}{k}) \sqrt{\frac{2\nu^2}{V\epsilon_0}} p(t) \cos(kz). \tag{2.2}$$

In these two expression, the wave number is given by $k = \nu/c$ with $\nu$ as frequency of the cavity mode, and $V$ is the effective cavity volume. $\epsilon_0$ denotes the electric permittivity and $\mu_0$ the magnetic permeability. The introduced canonical variables $p(t)$ and $q(t)$ fulfil the relation $p(t) = \dot{q}(t)$, thus the Hamiltonian describing the system can be written as

$$
\begin{aligned}
H &= \frac{1}{2}\int[\epsilon_0 E_x^2(z,t) + \frac{1}{\mu_0}B_y^2(z,t)]\mathrm{d}V \\
&= \frac{1}{2}(p^2 + \nu^2 q^2). \qquad (2.3)
\end{aligned}
$$

This expression is similar to the harmonic oscillator Hamiltonian $\hat{H} = \frac{1}{2}(\hat{p}^2 + \omega^2\hat{q}^2)$. Introducing the operators $\hat{p}$ and $\hat{q}$, which fulfil the relation $[\hat{q}, \hat{p}] = i\hbar$, quantizes the electromagnetic field from equation 2.3. By defining the creation operator $\hat{a}^\dagger$ and annihilation operator $\hat{a}$

$$
\begin{aligned}
\hat{a} &= \frac{1}{\sqrt{2\hbar\nu}}(\nu\hat{q} + \mathrm{i}\hat{p}), \qquad (2.4) \\
\hat{a}^\dagger &= \frac{1}{\sqrt{2\hbar\nu}}(\nu\hat{q} - \mathrm{i}\hat{p}), \qquad (2.5)
\end{aligned}
$$

the Hamiltonian can be expressed as

$$
\begin{aligned}
\hat{H} &= \hbar\nu(\hat{a}^\dagger\hat{a} + \frac{1}{2}) \qquad (2.6) \\
&= \hbar\nu(\hat{n} + \frac{1}{2}). \qquad (2.7)
\end{aligned}
$$

With these to operators forming the number operator $\hat{n} = \hat{a}^\dagger\hat{a}$, the Fock states are introduced.

### 2.1.2 Fock states

Fock states, or number states, are denoted as $|n\rangle$ and are eigenstates to the number operator $\hat{n}$. It fulfils the equation

$$
\hat{n}|n\rangle = n|n\rangle. \qquad (2.8)
$$

Here, $n$ defines the number of photons in the Fock state $|n\rangle$. If annihilation or creation operator is applied to a Fock state, the state can be raised or lowered

$$
\begin{aligned}
\hat{a} &= \sqrt{n}\,|n-1\rangle\,, \qquad (2.9) \\
\hat{a}^\dagger &= \sqrt{n+1}\,|n+1\rangle\,. \qquad (2.10)
\end{aligned}
$$

The annihilation operator decreases the Fock state by one, while the creation operator increases it by one. A state with $n = 0$ corresponds to the so called vacuum state $|0\rangle$. This vacuum state is the ground state of the harmonic oscillator and the lowest possible energy level. It is possible to create any Fock state by applying the creation operator to the ground state

$$|n\rangle = \frac{(\hat{a}^\dagger)^n}{\sqrt{n!}} |0\rangle . \tag{2.11}$$

Inserting the vacuum state $|0\rangle$ into the harmonic oscillator equation 2.7 leads to

$$\langle 0| \hat{H} |0\rangle = \hbar\nu \langle 0| (\hat{n} + \frac{1}{2}) |0\rangle = \frac{\hbar\nu}{2}, \tag{2.12}$$

which is a non-zero energy in the ground state. This energy leads to quantum noise.

### 2.1.3 Coherent states

Here, Fock states describe an quantum state with a well defined number of photons. For laser light, this condition is not given and Fock states are insufficient to describe it. However, a laser beam can be described with a coherent state. Photons contained in a coherent state are described in a Possionian distribution with the average photon number $\bar{n} = |\alpha|^2$ and variance $\langle\alpha\rangle = |\alpha|^2$, where $\alpha$ is a complex number. The coherent states are described through eigenvalues of the creation and annihilation operators

$$\hat{a} |\alpha\rangle = \alpha |\alpha\rangle , \tag{2.13}$$

$$\langle\alpha| \hat{a}^\dagger = \langle\alpha| \alpha^*, \tag{2.14}$$

where the eigenvalues $\alpha$ and $\alpha*$ are given by complex numbers. By applying the displacement operator $\hat{D}(\alpha) = \mathrm{e}^{\alpha\hat{a}^\dagger - \alpha^*\hat{a}}$ to the vacuum state, a coherent state can be generated

$$|\alpha\rangle = \hat{D}(\alpha) |0\rangle . \tag{2.15}$$

The coherent state can also be described as a superposition of Fock states

$$|\alpha\rangle = \mathrm{e}^{-\frac{1}{2}|\alpha|^2} \sum_{n=0}^{\infty} \frac{\alpha^n}{\sqrt{n!}} |n\rangle . \tag{2.16}$$

### 2.1.4 Heisenberg's uncertainty principle

Before introducing squeezed states of light, the Heisenberg's uncertainty principle needs to be recalled. The uncertainty principle states, that two non-commuting operators can't be measured simultaneously with an arbitrary precision. More specific, two observables $\hat{A}$ and $\hat{B}$, who fulfil the commutation relation $\left[\hat{A},\hat{B}\right] = \hat{C}$, have to obey the uncertainty relation

$$\Delta^2\hat{A}\cdot\Delta^2\hat{B} \geq \frac{1}{4}\left|\langle\left[\hat{A},\hat{B}\right]\rangle\right|^2 . \tag{2.17}$$

To be able to calculate the uncertainty relation for coherent and vacuum states, the quadrature operators $\hat{X}_1$ and $\hat{X}_2$ have to be defined. Defining them as

$$\hat{X}_1 = \hat{a} + \hat{a}^\dagger, \tag{2.18}$$

$$\hat{X}_2 = i(\hat{a}^\dagger - \hat{a}) \tag{2.19}$$

leads to the commutator

$$\left[\hat{X}_1,\hat{X}_2\right] = 2i \tag{2.20}$$

and uncertainty relation

$$\Delta^2\hat{X}_1\Delta^2\hat{X}_2 \geq 1. \tag{2.21}$$

These results hold for all orthogonal quadratures, since no assumptions about the quantum state were made to calculate the commutator $\left[\hat{X}_1,\hat{X}_2\right]$. In different manuscripts, the quadratures may be named $\hat{X}$, $\hat{Y}$ and may be defined with a different factor, which does not change the physical statement. Using these expressions for coherent or vacuum states, the uncertainty relation calculates to

$$\Delta^2\hat{X}_1\Delta^2\hat{X}_2 = 1. \tag{2.22}$$

Thus, they are called minimum uncertainty states.

## 2.2 Squeezed states of light

A special case of minimum uncertainty states are squeezed states of light. They obey the uncertainty relation 2.22, but one variance is smaller than the ground state variance, while the orthogonal variance is increased:

$$\Delta^2 \hat{X}_1 < 1 \tag{2.23}$$

$$\Delta^2 \hat{X}_2 = \frac{1}{\Delta^2 \hat{X}_1} > 1. \tag{2.24}$$

Mathematically, a squeezed state is generated by applying the squeeze operator $\hat{S}$ to the ground state $|0\rangle$. The operator is defined as

$$\hat{S} = \exp\left[\frac{1}{2}\xi^* \hat{a}^2 - \frac{1}{2}\xi \hat{a}^{\dagger 2}\right], \tag{2.25}$$

with $\xi = r \exp^{i2\Theta}$. In this expression, $r$ denotes the squeeze parameter and the squeeze angle is given by $\Theta$, which defines the squeezed state's orientation in the phase space. For $\Theta = 0$ follows

$$\Delta^2 \hat{X}_1 = e^{-2r}, \tag{2.26}$$

$$\Delta^2 \hat{X}_2 = e^{+2r}, \tag{2.27}$$

where $\Delta^2 \hat{X}_1$ is the squeezed (decreased) variance, while $\Delta^2 \hat{X}_2$ denotes the anti-squeezed (increased) variance. A different squeezed quadrature operator $\hat{X}_\Theta$ with a corresponding orthogonal anti-squeezed quadrature operator $\hat{X}_{\Theta+\pi/2}$ can be obtained changing the squeeze angle.

## 2.3 Phase space representation

A visualization of squeezed states can be given in the phase space, which is spanned by the amplitude quadrature operator $\hat{X}_1$ and phase quadrature operator $\hat{X}_2$. Figure 2.1 shows on the left a vacuum state in the phase space representation with an uncertainty depicted by a blue circle. On the right, a coherent state is depicted, which is displaced by the amplitude $\alpha$ from the vacuum state. In figure 2.2, both states are squeezed along the amplitude quadrature. Here, the corresponding uncertainties are

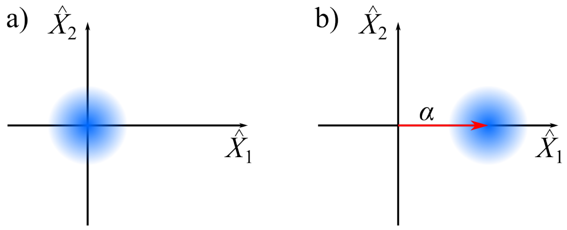

**Fig. 2.1: Representation of a vacuum and squeezed state in the phase space.** On the left, a vacuum state is depicted. The coherent state on the right is displaced by the amplitude $\alpha$ with respect to the vacuum state. In both states the uncertainty is depicted by a blue circle.

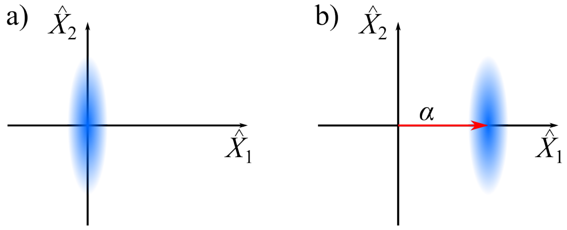

**Fig. 2.2: Representation of squeezed states in the phase space.** Compared to figure 2.1, the vacuum and coherent state are squeezed along the amplitude quadrature. The corresponding uncertainties are depicted with ellipses.

depicted by ellipses with a semi minor axis along the $\hat{X}_1$ axis, indicating the squeezed quadrature. Accordingly, the semi-mayor axis lays on the $\hat{X}_2$ axis.

These representations are a projection of Wigner functions on a 2D plane. A Wigner function gives a full representation of a quantum state and is defined by the integral

$$W(X_1, X_2) = \frac{1}{2\pi\hbar}\int_{-\infty}^{\infty} \langle X_1 + \frac{x}{2}|\,\hat{\rho}\,|X_1 - \frac{x}{2}\rangle\, \mathrm{e}^{\frac{-\mathrm{i}X_2 x}{\hbar}}\,\mathrm{d}x. \tag{2.28}$$

In this expression, $\hat{\rho}$ denotes the density operator of the system. As a so called quasi-probability function, the Wigner function allows negative values, for instance in the case of the Fock state $|1\rangle$ [Bau16, p.8-10]. To obtain a probability distribution for the phase or amplitude quadrature operator, the Wigner function has to be integrated over the orthogonal quadrature operator

$$p(X_1) = \int_{\infty}^{\infty} W(X_1, X_2)\mathrm{d}X_2, \tag{2.29}$$

$$p(X_2) = \int_{\infty}^{\infty} W(X_1, X_2)\mathrm{d}X_1. \tag{2.30}$$

Figure 2.3 displays a Wigner function for a vacuum and a squeezed state. The vacuum state is clearly rotationally symmetric and the variance along every axis is 1. In contrast, the squeezed state does not show a rotational symmetry. A squeeze factor of 4 (= 6 dB) is displayed as an example, leading to a four times smaller squeezed variance for the amplitude quadrature compared to the vacuum state. Accordingly, the phase quadrature's variance shows an increase by a factor of 4.

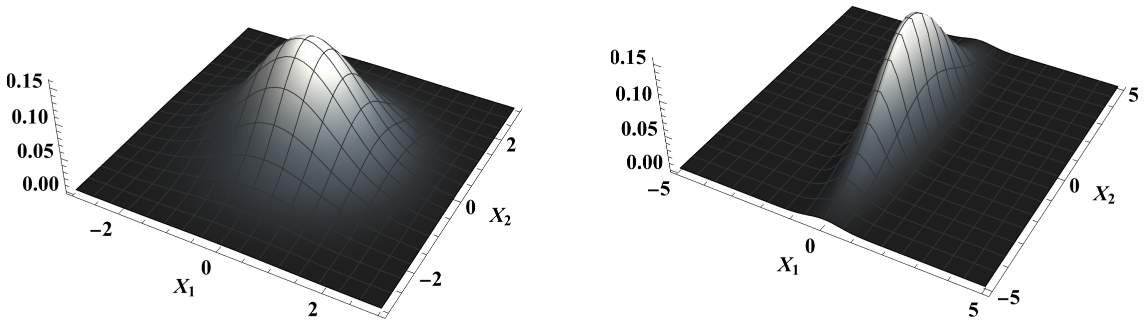

(a) Wigner function of a vacuum state.

(b) Wigner function of an amplitude-squeezed vacuum state.

**Fig. 2.3: Wigner function of vacuum state and a squeezed vacuum state.** A vacuum state is depicted on the left. The rotational symmetry leads to variances equal to one along all projection angles. A squeezed state with a squeeze factor of 4 (= 6 dB) is shown on the right, where the function shows no rotational symmetry. The squeezed amplitude quadrature's variance is 4 times smaller compared to the vacuum, whereas the anti-squeezed phase quadrature's variance increases by the factor 4.

## 2.4 Light fields in the phasor picture

Light field modulations, for instance a phase or amplitude modulation, can be intuitively visualized in the phasor picture [Mal06]. In this picture, squeezed states of light can be understood as side bands at frequencies $\pm\Omega$ modulated on a carrier field with the frequency $\nu_0$ [Sch17]. The importance of this description becomes clear considering the measurement process of squeezed states of light in an experiment, which is always performed at a side band frequency $\Omega$ within a bandwidth $\Delta\Omega$. However, in the description of the phasor picture the bandwidth is considered to be infinitesimal small.

In the classical description of light, an electric field can be described by

$$E(t) = E_0 e^{i\nu_0 t} \tag{2.31}$$

with the amplitude $E_0$ and phase $\nu_0 t$, which is rotating in the complex plane. To obtain a stationary illustration, the field is observed in the rotating frame picture, where the coordinate system rotates with the same frequency $\nu_0$. As a result, all fields with a frequency $\Omega \neq \nu_0$ will rotate clockwise for $(\nu_0 > \Omega)$ or counter clockwise for $(\nu_0 < \Omega)$. A superposition of light fields with different frequencies in this picture is simply given by the superposition of the phasors. Each of these phasors is rotating with their own frequency $\nu_0 \pm \Omega$.

### 2.4.1 Amplitude modulation

Considering a sinusoidal modulation only acting on the amplitude of a light field $E(t) = E_0 e^{i\nu_0 t}$, the resulting field can be written as

$$\begin{aligned} E_{AM}(t) &= E_0(1 + m\cos(\Omega t))e^{i\nu_0 t} && (2.32) \\ &= E_0\Big(e^{i\nu_0 t} + \frac{m}{2}e^{i(\nu_0+\Omega)t} + \frac{m}{2}e^{i(\nu_0-\Omega)t}\Big) && (2.33) \end{aligned}$$

with the modulation depth $m$ and modulation frequency $\Omega$. The field $E_AM$ can be understood as sum of a carrier field with the frequency $\nu_0$ and side bands with an amplitude of $\frac{E_0 m}{2}$ at the frequencies $\nu_0 \pm \Omega$. Those side bands are usually referred as *upper* $(\nu_0 + \Omega)$ and *lower* $(\nu_0 - \Omega)$ side band. Figure 2.4 depicts the amplitude modulation on a carrier field in phasor diagrams at different points in time. Those points in time refer to the distinct side band phases of 0, $\pi/2$, $\pi$ and $3\pi/2$ with respect to the carrier field. The lower diagrams display the superposition of the three light fields, resulting in an oscillating amplitude.

### 2.4.2 Phase modulation

A modulation with a frequency $\Omega$ and depth $m$ only acting on the phase of a light field $E(t) = E_0 e^{i\nu_0 t}$ is mathematically described by

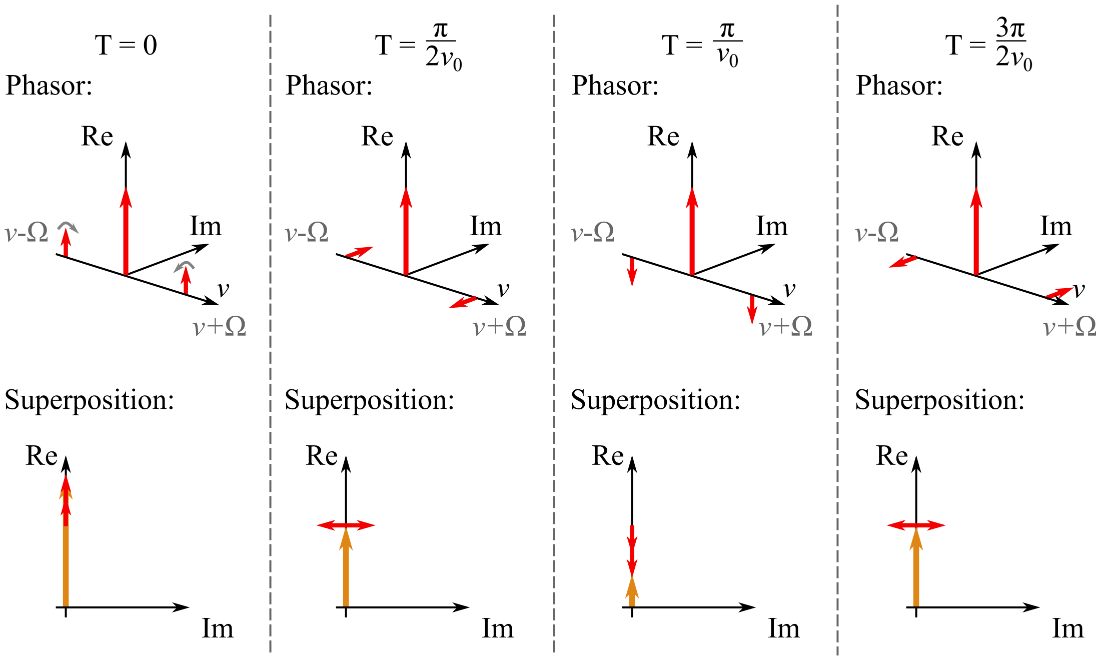

**Fig. 2.4: Amplitude modulation in the phasor picture.** In the upper panel, the time evolution of the side bands are shown in the rotating frame with frequency $\nu_0$. The side bands represented by the small red arrows at the frequencies $\nu_0 \pm \Omega$ rotate clockwise (lower side band)or counter-clockwise (upper side band) in time. In this rotating frame, the carrier field (large red arrow) stays stationary. The superposition of carrier field and side bands is depicted in the lower panels by an orange arrow, which clearly indicates an oscillating amplitude with a stationary phase in the time evolution. Here, the phasor for the carrier field is not shown.

$$\begin{aligned}
E_{PM}(t) &= E_0 e^{i(\nu_0 t + m\cos(\Omega t))} && (2.34)\\
&= E_0 e^{i\nu_0 t}\left[J_0(m) + \sum_{j=1}^{\infty} i^j J_j(m)(e^{ij\Omega t} + e^{-ij\Omega t})\right] && (2.35)\\
&= E_0 e^{i\nu_0 t}[J_0(m) + iJ_1(m)e^{i\Omega t} + iJ_1(m)e^{-i\Omega t} + \mathcal{O}(m^2)] && (2.36)\\
&\approx E_0\left[e^{i\nu_0 t} + i\frac{m}{2}e^{i(\nu_0+\Omega)t} + i\frac{m}{2}e^{i(\nu_0-\Omega)t}\right] && (2.37)
\end{aligned}$$

with the Bessel functions $J_j(m)$ of the $j$-order. The approximation in the fourth line is only valid for small modulation depths $m << 1$. Otherwise, higher order side bands with frequencies $\pm n\Omega$ are generated. Due to this limitation, only two side bands at the frequencies $\nu_0 \pm \Omega$ are created with an amplitude of $i\frac{E_0 m}{2}$. Compared to the amplitude modulation, the side bands are phase shifted by $\pi/2$ with respect to the carrier field. In the superposition of the fields, this phase shift leads to an oscillation of the phase while the amplitude remains constant. In figure 2.5, the

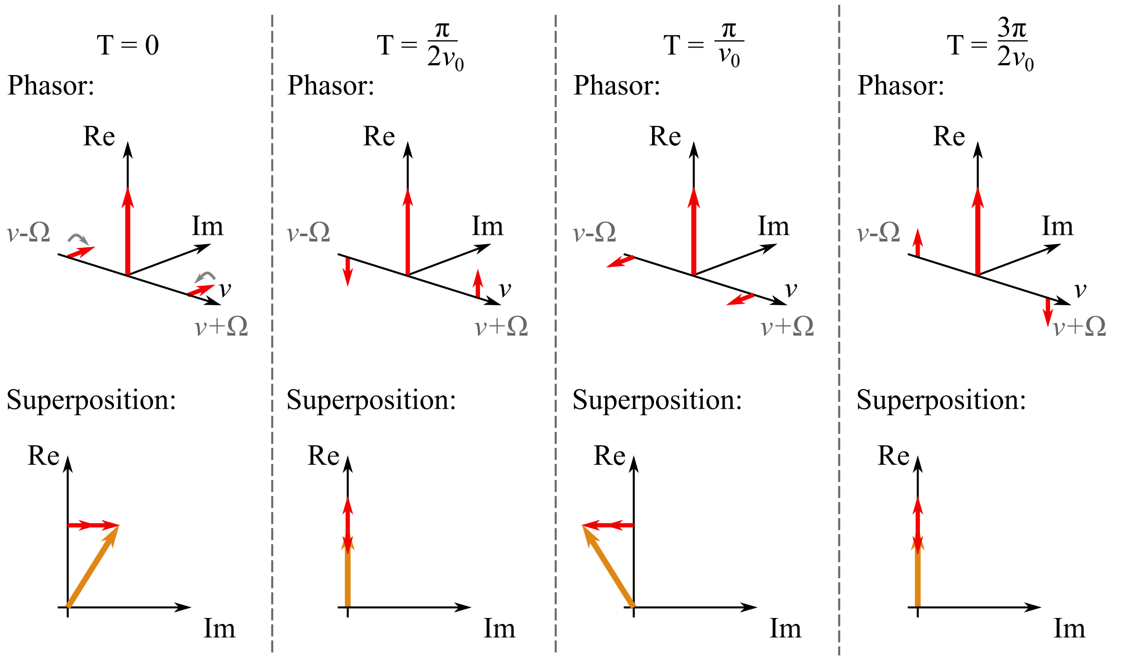

**Fig. 2.5: Phase modulation in the phasor picture.** The upper panels show the time evolution of the side bands in the rotating frame with frequency $\nu_0$. Small red arrows indicate the side bands at the frequencies $\nu_0 \pm \Omega$, which rotate clockwise (lower side band) and counter-clockwise (upper side band) in time. The carrier field depicted by a large arrow stays stationary. The lower panel shows the superposition and the time evolution of the phase modulated field depicted by an orange arrow. Here, only the side bands and not the carrier field are shown. As a result, the field only oscillates in the phase while the amplitude stays stationary.

phase modulation is depicted in the phasor picture as well as the superposition of the carrier field with the side bands.

## 2.4.3 Quantum noise in the phasor picture

In order to illustrate quantum noise in the phasor picture, the phase space spanned by amplitude and phase operator is considered instead of the complex plane in the description of modulations. In the phase space, every side band has an uncertainty in each quadrature operator with the variance of 1/2, which is the quantum noise on every side band frequency. Without a carrier field, those uncertainties correspond to the quantum noise of the vacuum. Upon a measurement at a distinct side band frequency, the side bands with the noise are summed up and the double sided phasor picture becomes a single sided phasor picture. Thus, the variances of the quadrature operators are equal to one again, as introduced before for minimum uncertainty states. Figure 2.6 illustrates the quantum noise of a vacuum state at a side band frequency of $\pm\Omega$ in the double sided and single sided phasor picture.

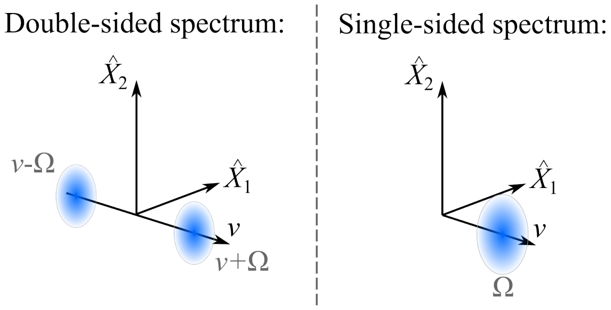

**Fig. 2.6: Vacuum noise in the phasor picture.** The uncertainties of the side bands at the frequencies $\nu_0 \pm \Omega$ for a vacuum state are depicted by blue circles. For every point in time, the double sided phasor picture looks like the left panel with quadrature variances of the value 1/2. In the single sided phasor picture on the right panel, the variances add up to 1.

In the case of squeezed fields, the photons in the upper and lower side bands are correlated with thermally excited uncertainties. The uncertainties of a side band pair at frequency $\Omega$ show correlations as well as anti-correlations. Due to these correlations, the field results in having a squeezed quadrature with an orthogonal anti-squeezed quadrature. The orientation of the squeeze angle depends on the phase of the side bands with respect to the carrier field, analogous to the phase and amplitude modulation. Without a carrier field at frequency $\nu_0$, the quantum noise of the vacuum is squeezed. Since the vacuum does not have a distinct phase, the phase of the side bands and therefore the squeeze angle have to be referenced to an auxiliary field. Figure 2.7 depicts an amplitude squeezed vacuum state in the phasor picture. The correlations are marked with + and ∘. Analogous, a phase squeezed vacuum state is illustrated in figure 2.8.

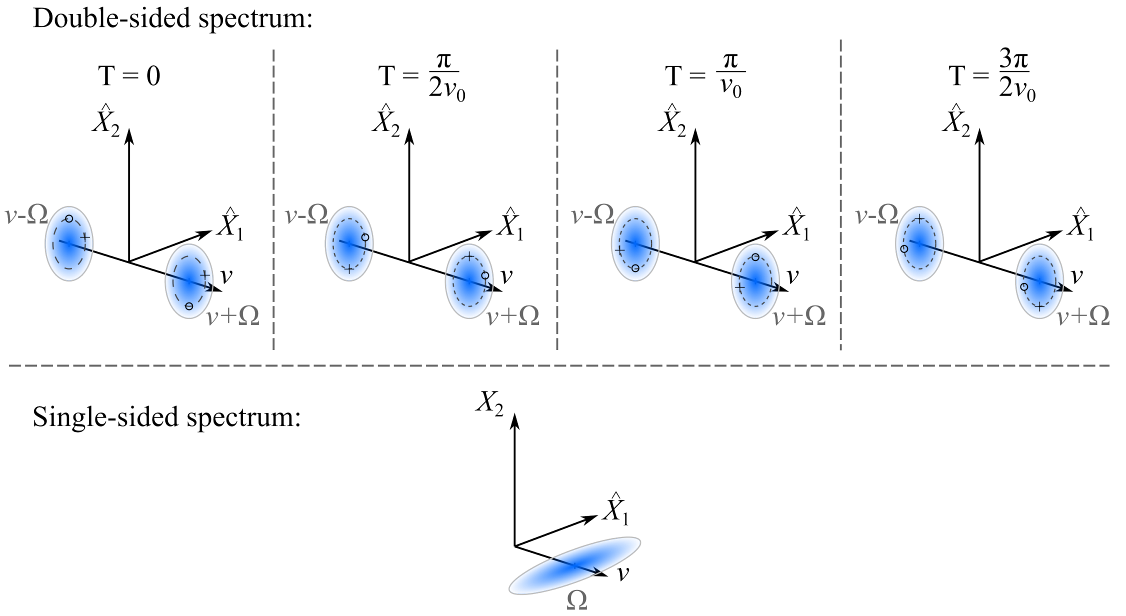

**Fig. 2.7: Amplitude squeezed vacuum state in the phasor picture.** The upper panel shows the time evolution of the side bands at frequencies $\nu_0 \pm \Omega$ with quantum noise depicted by blue circles in the two sided phasor picture for a vacuum state. The lower side band rotates clockwise, while the upper one rotates counter-clockwise. Correlations in the thermally excited quantum noise are depicted by $+$ and $\circ$. In the single sided phasor picture displayed in the bottom panel, the variance of the amplitude quadrature is squeezed while the phase quadrature is anti-squeezed due to the correlation in the quantum noise.

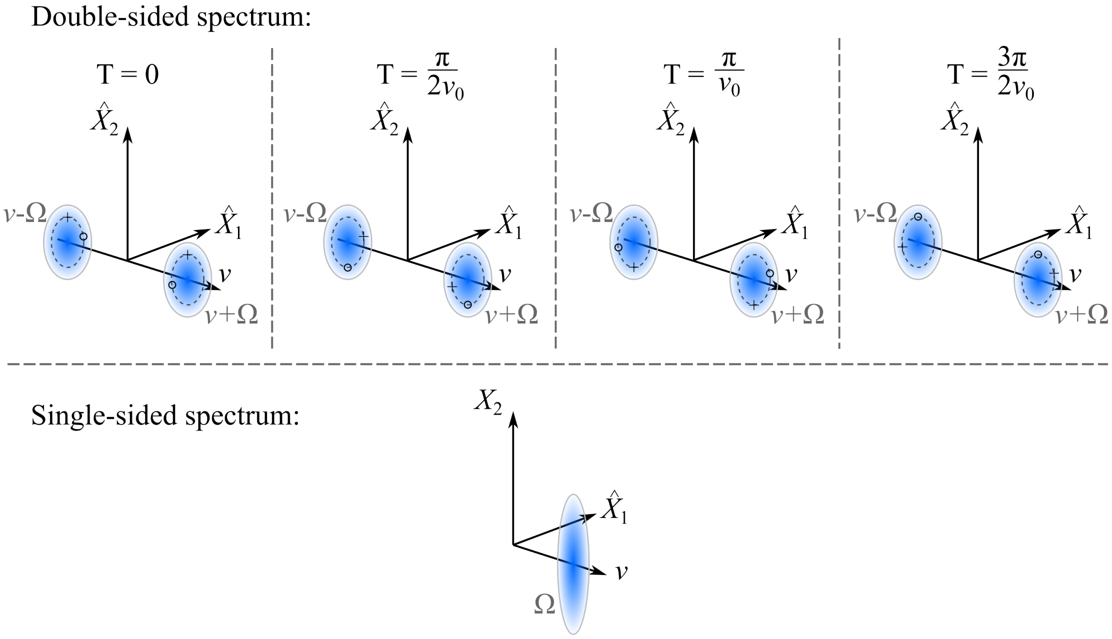

**Fig. 2.8: Phase squeezed vacuum state in the phasor picture.** In the upper panel, the time evolution of the side bands at frequencies $\nu_0 \pm \Omega$ with quantum noise depicted by blue circles are illustrated in the double sided phasor picture for a phase squeezed vacuum state. The upper side band rotates counter-clockwise and the lower side band rotates clockwise. The quantum noise is thermally excited and correlations are marked by $+$ and $\circ$. On contrast to the amplitude squeezed state, the side bands are phase shifted by $\pi/2$. In the single sided phasor picture, the correlations in the quantum noise result in a squeezed phase quadrature and anti-squeezed amplitude quadrature.

## 2.5 Effect of optical loss on squeezed states

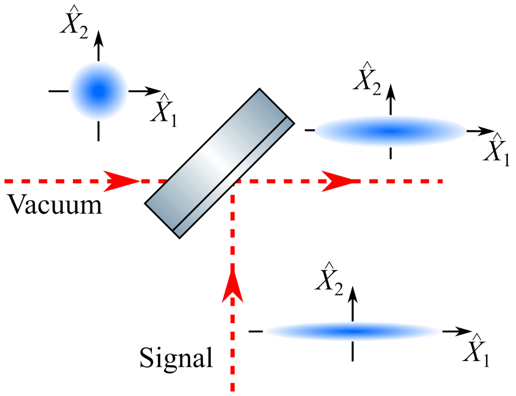

**Fig. 2.9: Effect of optical loss on squeezed states visualized by a beam splitter model.** The squeezed state depicted as a blue ellipse gets superposed with a vacuum state depicted by a blue circle on a beam splitter. In this picture, the coupling of the vacuum state to the squeezed state depends on the transmittance. As a result, the squeezed state has a decreased squeeze factor depicted by a less slim ellipse. The empty port of the beam splitter can be neglected for this model.

In every experiment, optical losses couple into the light field. Those losses can origin, for instance, from absorptions or scattering of imperfect optics. While optical loss shows only a reduction of the amplitude for coherent states, squeezed states experience a reduction of the squeeze factor. The effect of losses can be modelled as a superposition of the squeezed field with a vacuum field on a beam splitter, which is depicted in figure 2.9. Since the vacuum state's quadrature variance is larger compared to the squeezed state, the superposition results in an increased variance $\Delta^2\hat{X}_{\Theta,loss}$ with respect to the squeezed state's variance $\Delta^2\hat{X}_{\Theta}$. The increased variance can be expressed by

$$\Delta^2\hat{X}_{\Theta,loss} = (1-\eta)\cdot\Delta^2\hat{X}_{\Theta} + \eta\cdot\Delta^2\hat{X}_{Vac} \tag{2.38}$$

where $\eta$ represents the losses. In this beam splitter model, $\eta$ is given by the beam splitter's transmittance $T$. Apart from imperfect optics, which could easily be modelled by the beam splitter analogy, non-optimal fringe contrast of overlapping modes and detection inefficiencies also contribute to losses. Figure 2.10 shows a simulation how the total optical loss in a system affects the squeezed and anti-squeezed noise powers referenced to the vacuum for different initial squeeze factors. Noticeable is the way stronger influence of losses on the squeezed states compared to the anti-squeezed states. This effect can be explained by the relation between vacuum noise

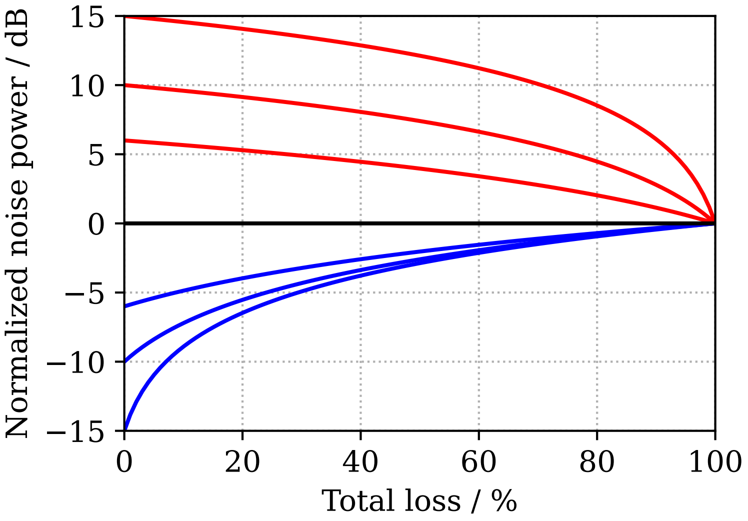

**Fig. 2.10: Simulation of the effect of total optical loss on squeezed noise normalized to the vacuum.** The effect of loss is simulated for squeezed states according to equation 2.38 with initial squeeze factors of 6 dB, 10 dB and 15 dB in the blue traces. Corresponding anti-squeeze states are shown in red. All traces are normalized to the vacuum noise. Evidently squeezed states are more strongly effected by optical loss compared to anti-squeezed states. It is crucial to minimize loss to obtain high squeeze factors.

and squeezed- / anti-squeezed noise. The vacuum noise has a much larger effect on the relatively small squeezed noise in contrast to the anti-squeezed noise, which is relatively much larger than the vacuum noise. Therefore it is crucial to minimize losses in the experiment to detect high squeeze factors. More precisely, losses need to be less than 10% to achieve squeeze factors of 10 dB.

## 2.6 Non-linear processes

Crucial for the generation of squeezed states of light in this work is the second-harmonic generation and parametric down-conversion. To explain these two processes, higher order polarisation effects in media need to be taken into account. When an electro-magnetic wave enters a medium, the charge inside starts to oscillate. These oscillation can be described by the Polarization $P(t)$, which can be written in the following power series

$$P(t) = \epsilon_0(\chi^{(1)}E(t) + \chi^2 E(t)^2 + \chi^3 E(t)^3 + ...). \tag{2.39}$$

$\epsilon_0$ denotes the permittivity in the vacuum, $E(t)$ is the electric field strength, and $\chi^{(i)}$ is the i-th order susceptibility, which is a material parameter. The non-linear term

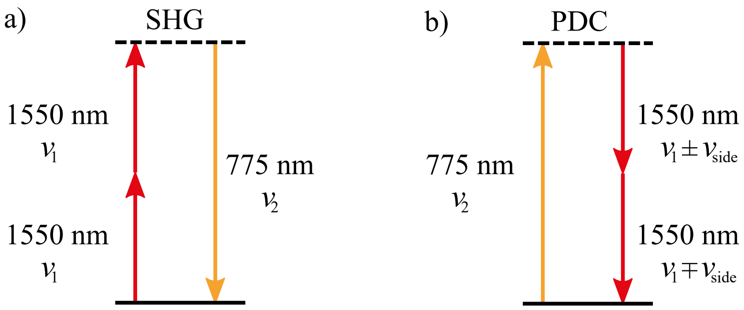

**Fig. 2.11: Energy level diagram of the second-harmonic generation and parametric down-conversion process.** The left side depicts the second-harmonic generation process. Two 1550 nm photons excite an atom to a virtual state, which decays by emitting a photon with the half wavelength 775 nm. On the right side, the reverse process is depicted. In the parametric down-conversion, a 775 nm photon excites an atom to a virtual energy level. It decays by emitting two photons at 1550 nm. The frequency of the generated photon might differ by a side band frequency $\nu_{\text{side}}$. To conserve the energy, both side band frequencies must add up to zero.

$P^{NL} = \chi^2 E(t)^2 + \chi^3 E(t)^3 + ...$ give rise to new frequency components [Boy08, pp.1-11]. In case of the second-harmonic generation, the input field with a frequency $\nu_1$ converts into a signal field with a doubled frequency $\nu_2 = 2\nu_1$. Thus, the energy conservation is not violated during the process. The parametric down-conversion process is the inverse to the second-harmonic generation and is utilized to generate squeezed vacuum states. For this purpose it is crucial to note, that the parametric down-conversion process is driven below the lasing threshold. A visualisation of second-harmonic generation and parametric down-conversion with the help of energy level diagrams is illustrated in figure 2.11. Building a cavity around the non-linear medium increases the electric field strength $E(t)$, which increases coupling between the light and the non-linear medium. Accordingly, the efficiency of both non-linear processes can be enhanced by a cavity.

## 2.7 Spectra of squeezed states from cavity-enhanced generation

Due to the generation of squeezed states in a cavity, the spectrum is limited by the cavity linewidth. The spectra for squeezed and anti-squeezed quadratures are described by the equation [Sch18]

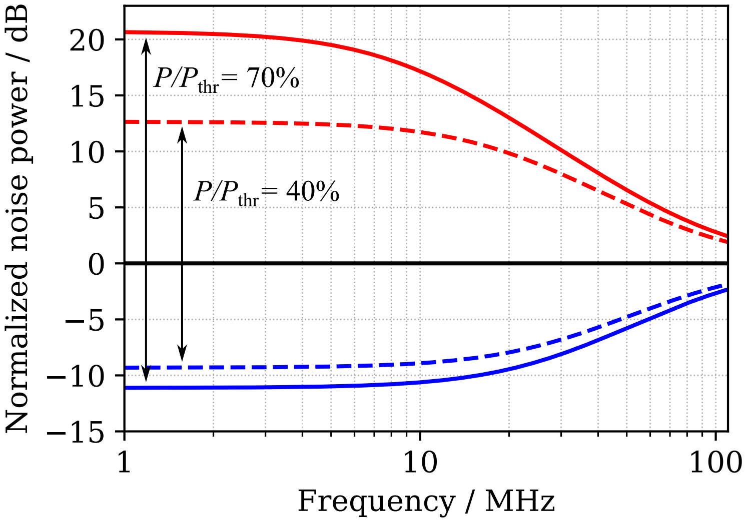

**Fig. 2.12: Vacuum-noise normalized spectrum of squeezed states generated by cavity-enhanced parametric down-conversion.** Spectra for the squeezed quadratures are displayed in blue traces, while the anti-squeezed ones are shown by red traces. An overall optical loss of 7% is assumed. The spectra at a pump power of $P/P_{\mathrm{thr}} = 70\%$ (solid traces) show increased squeezed and anti-squeezed factors compared to the spectra at a pump power of $P/P_{\mathrm{thr}} = 40\%$ (dashed traces). All spectra are clearly limited by the cavity linewidth of $\gamma/2\pi = 108\,\mathrm{MHz}$.

$$S_{\text{sqz, asqz}} = 1 \mp \eta \frac{4\sqrt{\frac{P}{P_{\mathrm{thr}}}}}{\left(1 \pm \sqrt{\frac{P}{P_{\mathrm{thr}}}}\right)^2 + 4\left(\frac{2\pi f}{\gamma}\right)^2}, \tag{2.40}$$

where $\gamma$ denotes the full width half maximum cavity linewidth, $\eta$ the detection efficiency, and $P_{\mathrm{thr}}$ the oscillation threshold. In figure 2.12, simulated spectra are shown for a cavity linewidth of $\gamma/2\pi = 108\,\mathrm{MHz}$, a loss of 7%, and pump powers of $P/P_{\mathrm{thr}} = 40\%$ and $P/P_{\mathrm{thr}} = 70\%$. An increased pump power results in higher squeezed and anti-squeezed factors. However, the effect more evident in the anti-squeezed quadrature, since the squeeze factors are more dominated by the optical loss.

## 2.8 Experimental techniques

### 2.8.1 Homodyne detection

The *balanced homodyne detection* can discriminate between amplitude and phase quadrature. Thus, it is able to detect squeezed states of light [GK05]. Hereby, the

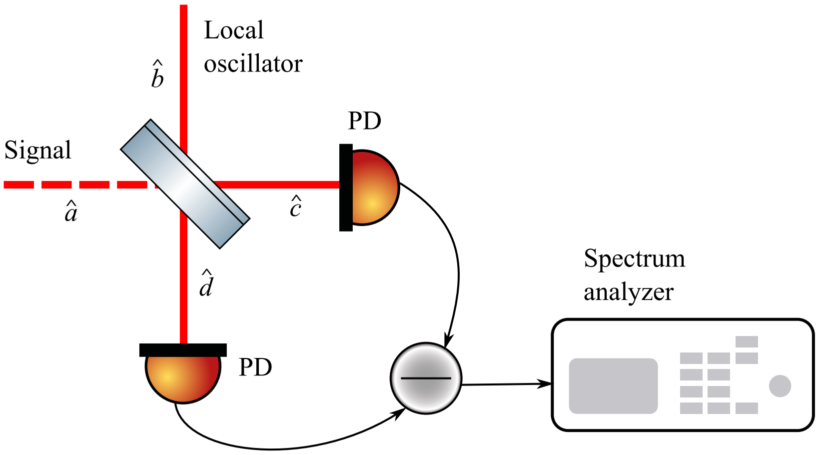

**Fig. 2.13: Schematic of the balanced homodyne detection.** Signal $\hat{a}$ and local oscillator field $\hat{b}$ are overlapped spatially on a 50:50 beam splitter. The output ports with the mixed signals $\hat{c}$, $\hat{d}$ are each detected with a photo diode and the resulting photo currents $I_{\hat{c}}$, $I_{\hat{d}}$ are subtracted from each other. A transimpedance amplifier converts the resulting current $I_{-}$ into a voltage signal, which can be read out with a spectrum analyzer

signal field containing the squeezed states of light is overlapped spatially with a strong coherent field called *local oscillator* on a balanced (50:50) beam splitter. A schematic is shown in figure 2.13. The output ports $\hat{c} = \langle \hat{c}^\dagger \hat{c} \rangle$ and $\hat{d} = \langle \hat{d}^\dagger \hat{d} \rangle$ are each detected with a photo diode. They measure the photo currents $I_{\hat{c}}$ and $I_{\hat{d}}$, which are subtracted by the detector to $I_{-} = I_{\hat{c}} - I_{\hat{d}}$. The output modes can be described by

$$\hat{c} = \sqrt{T}\hat{a} + \mathrm{i}\sqrt{1-T}\hat{b} \tag{2.41}$$

$$\hat{d} = \mathrm{i}\sqrt{1-T}\hat{a} + \sqrt{T}\hat{b}. \tag{2.42}$$

Since the transmittance $T$ of the beam splitter is equal to 0.5, it follows

$$\hat{c}^\dagger\hat{c} = \frac{1}{2}\hat{a}^\dagger\hat{a} + \frac{1}{2}\hat{b}^\dagger\hat{b} + \mathrm{i}\frac{1}{2}(\hat{a}^\dagger\hat{b} - \hat{b}^\dagger\hat{a}) \tag{2.43}$$

$$\hat{d}^\dagger\hat{d} = \frac{1}{2}\hat{a}^\dagger\hat{a} + \frac{1}{2}\hat{b}^\dagger\hat{b} - \mathrm{i}\frac{1}{2}(\hat{a}^\dagger\hat{b} - \hat{b}^\dagger\hat{a}) \tag{2.44}$$

and therefore $I_{-}$ can be written as

$$I_- = I_c - I_d = \langle \hat{c}^\dagger \hat{c} - \hat{d}^\dagger \hat{d} \rangle \tag{2.45}$$
$$= \mathrm{i} \langle \hat{a}^\dagger \hat{b} - \hat{b}^\dagger \hat{a} \rangle. \tag{2.46}$$

The $\hat{a}^\dagger \hat{a}$ and $\hat{b}^\dagger \hat{b}$ cancel out, which means no technical noise in the input fields is coupled into the measurement and only the interference terms $\hat{a}^\dagger \hat{b}$, $\hat{b}^\dagger \hat{a}$ remain. The local oscillator is a coherent field. Thus, it can be written as $\beta \mathrm{e}^{-i\nu t}$ with $\beta = |\beta| \, \mathrm{e}^{i\Phi}$. For the subtracted photo current follows

$$I_- = \mathrm{i} \langle \hat{a}^\dagger \hat{b} - \hat{b}^\dagger \hat{a} \rangle \tag{2.47}$$
$$= \mathrm{e}^{\mathrm{i}\frac{\pi}{2}} \langle \hat{a}^\dagger \, |\beta| \, \mathrm{e}^{\mathrm{i}\Phi} \mathrm{e}^{-i\nu t} - \hat{a} \, |\beta| \, \mathrm{e}^{-\mathrm{i}\Phi} e^{\mathrm{i}\nu t} \rangle \tag{2.48}$$
$$= |\beta| \, \langle \hat{a}^\dagger \mathrm{e}^{\mathrm{i}\Theta} \mathrm{e}^{-\mathrm{i}\nu t} + \hat{a} \mathrm{e}^{-\mathrm{i}\Theta} \mathrm{e}^{\mathrm{i}\nu t} \rangle \tag{2.49}$$

with $\mathrm{e}^{i\Theta} = \mathrm{e}^{i(\Phi + \frac{\pi}{2})}$. The Signal and local oscillator fields origin from the same source and have therefore the same frequency $\nu$. The signal field can be written as $\hat{a} = \hat{a}_0 \mathrm{e}^{-i\nu t}$, which results into

$$I_- = |\beta| \, \langle \hat{a}_0^\dagger e^{\mathrm{i}\Theta} + \hat{a}_0 e^{-\mathrm{i}\Theta} \rangle \tag{2.50}$$
$$= |\beta| \, \langle \hat{X}(\Theta) \rangle. \tag{2.51}$$

$\hat{X}(\Theta) = \hat{a}_0^\dagger e^{\mathrm{i}\Theta} + \hat{a}_0 e^{-\mathrm{i}\Theta}$ is the generalized quadrature operator. The signal of the homodyne detection scales with the amplitude $|\beta|$ of the local oscillator and by changing its phase, the readout angle $\Theta$ can be varied. Thus, an arbitrary quadrature of the signal field can be measured. A transimpedance amplifier converts the subtracted current $I_-$ into a voltage signal, which can be read out with a spectrum analyser. The measured noise power is proportional to the squeezed state's variance [Sch17, p. 17]. In this detection scheme, the detection efficiency strongly correlates with the overlap of signal and local oscillator field, and the quantum efficiency of the photodiodes. The spatial overlap can be characterized by the fringe visibility, which is given by

$$V = \frac{I_{max} - I_{min}}{I_{max} + I_{min}} \tag{2.52}$$

for equal light field intensities at the input ports [Kha11, p.39]. $I_{max}$ and an $I_{min}$

correspond to the maximum and minimum intensities measured at one photo diode due to constructive or destructive interference of the light fields. For a visibility $V = 1$, both light fields are perfectly overlapped resulting in a maximal interference signal. However, the overlap is not perfect in general in an experiment and the visibility is $V < 1$. Including the quantum efficiency of the photo diodes, the overall detection efficiency of the homodyne detector can be written as [Wad16, p.149]

$$\eta_{det} = \eta_{PD} V^2 \tag{2.53}$$

### 2.8.2 Phase matching

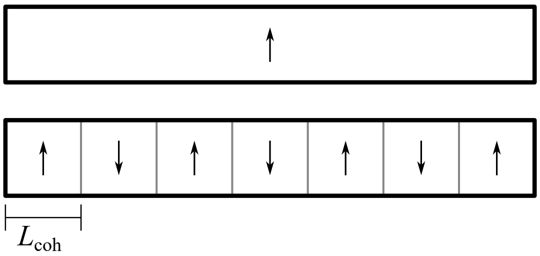

**Fig. 2.14: Non-linear crystal with and without periodic poling.** In periodically poled non-linear crystal (bottom) the sign of effective non-linearity $d_{eff}$ changes periodical with the coherence length. Thus, a quasi phase matched system is achieved and the second-harmonic intensity increases over the whole crystal length. With a constant $d_{eff}$, the birefringence of crystal has to be used to achieve a phase matching [Boy08, p.85].

Both non-linear processes take place inside a non-linear crystal. Due to the dispersion of light inside a medium, fundamental and second-harmonic field travel with different velocities inside the crystal. Therefore, a phase matching is needed for the fields to travel at the same speed. Since the conversion takes place at every point in the crystal, the phase matching ensures a constructive interference between the generated second-harmonic waves, which results in an increased field strength. The phase mismatch can be written as

$$\Delta k = 2k_1 - k_2 \tag{2.54}$$

with $k_i$ being the wave number of the corresponding field [Boy08]. This condition also holds for degenerate down-conversion [Vah08, p.29]. Considering a perfect phase matching, where $n_1 = n_2$ and $\nu_2 = 2\nu_1$ is fulfilled, the phase matching condition can be written as

$$\Delta k = 2k_1 - k_2 = 0 \tag{2.55}$$

$$\Leftrightarrow \frac{n_2 \nu_2}{c_2} = 2\frac{n_1 \nu_1}{c_1}. \tag{2.56}$$

A perfect phase matching can be achieved in a birefringent non-linear medium, where ordinary and extraordinary axis have different refractive indices. In practice, it is complicated to realize, since the effect only arises under one incident angle between pump beam and crystal. Therefore, the quasi phase matching method is used for the experiments in this thesis. In this method, the crystal is segmented in domains, where the sign of the effective non-linearity $d_{eff}$ alternates. Figure 2.14 depicts a periodically poled crystal in comparison to a normal one. The sign change leads to phase change of $\pi$ for generated waves in neighbouring domains. In combination with a domain length given by the coherence length $L_{\mathrm{coh}}$, second harmonic waves generated in different domains interfere constructively. The effect is depicted in figure 2.15. In red, the case of no phase matching is shown, where destructive interference prevents an amplification. The quasi phase matched system in orange leads to a constructive interference and an amplification of the second harmonic field. Compared to the perfectly phase matched system in blue, the built up in a quasi phase matched system is not strictly monotonous. In the experiment, the domain length is fine tuned by heating the crystal, exploiting the thermal dependence of the refractive index, which varies the optical path length inside the crystal. Taking Gaussian beams into account, the phase matching values become non-zero due to the Gouy phase [LS07]. Those can also be compensated for by thermally fine tuning the domain length.

### 2.8.3 Pound-Drever-Hall control loop

In experiments with cavities, especially multiple cavities, it is crucial to implement a control loop to hold them on resonance. One way to vary the cavity length is by actuating a mirror mounted on a piezo-electric element. However, a control loop can not minimize a signal only by measuring it in reflection of the cavity, due to the symmetry of the resonance peak. If the signal diverts from the minimum, there is no information on whether the cavity length has to be decreased or increased. This problem also remains, if it is desired to maximize the signal in transmission of a cavity.

The Pound-Drever-Hall control loop [Bla01] provides a solution by implementing a phase modulation of the frequency $\Omega$ with an electro-optical modulator (EOM). This way, a lower and an upper side band is generated. Upon reflection, those side bands

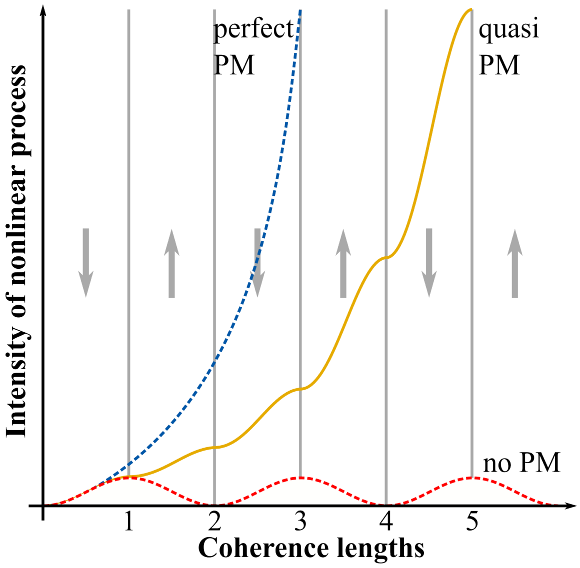

**Fig. 2.15: Illustration of a second-harmonic built-up in a quasi phase matched system.** In case of no phase matching (red), the system does not lead to an amplification of the second-harmonic. The different velocities of fundamental and second harmonic field lead to a de-constructive interference and thus to an oscillating signal. A quasi phase matched system (orange) leads to build-up inside the crystal. Compared to a perfect phase matched system (blue), the built-up is not strictly monotonous.

experience a different phase change with respect to carrier field, resulting in a beat signal between carrier light and side bands as well as between the side bands. To gain information on the phase of the beat pattern, the light has to be detected with a photo diode, where the signal is demodulated at a proper phase with an electronic modulation of the frequency $\Omega$. Here, a low pass filter has to cut off signals at $2\Omega$, as they correspond to the beat between the two side bands. As a result, a signal with a zero-crossing corresponding to the carrier light's phase is generated. Thus, information for adjusting the cavity length is given. This signal can be fed back to the piezo-electric element controlling the cavity length, after sending it through a proportional-integral-derivative controller for frequency dependent shaping.

# Chapter 3

# Generation of a squeezed vacuum state of light with a monolithic cavity

In this chapter, a monolithic cavity design solely consisting of one ppKTP crystal with curved and coated end faces was investigated for a possible application in future compact sources for squeezed states of light. Compared to designs with additional mirrors aside from the crystal, there were no cavity internal anti-reflective (AR) coatings contributing to loss reducing the squeeze factor. Additionally, the cavity's mechanical stability was increased by its single-piece construction. The potential of monolithic resonators for the generation of squeezed states of light had already been a subject of research. The first squeeze factor of 10 dB was observed in a setup utilizing this cavity design at a wavelength of 1064 nm [VMC$^+$08] and later squeeze factors up to 12.7 dB [Ste13, p.51]. The monolithic design allows for cavities with a length of a a few Millimetres, which led to the observation of squeezed vacuum states in the Gigahertz range at a wavelength of 1550 nm utilizing a 2.3 mm long cavity [AMS13]. Studies to generate squeezed states of light in the optical wavelength range [YNF10], [ZM18] and to generate bright squeezed states of light were conducted utilizing monolithic cavities [KPFM93]. However, in the squeezed vacuum generation studies, only the PDC process was amplified by a monolithic cavity, while the second harmonic pumping light was generated in a non-monolithic cavity. In the study presented here, the SHG and PDC process were each cavity-enhanced by a doubly-resonant monolithic cavity to generate squeezed vacuum states of light at 1550 nm. This research was a continuation of my master thesis [Hag19].

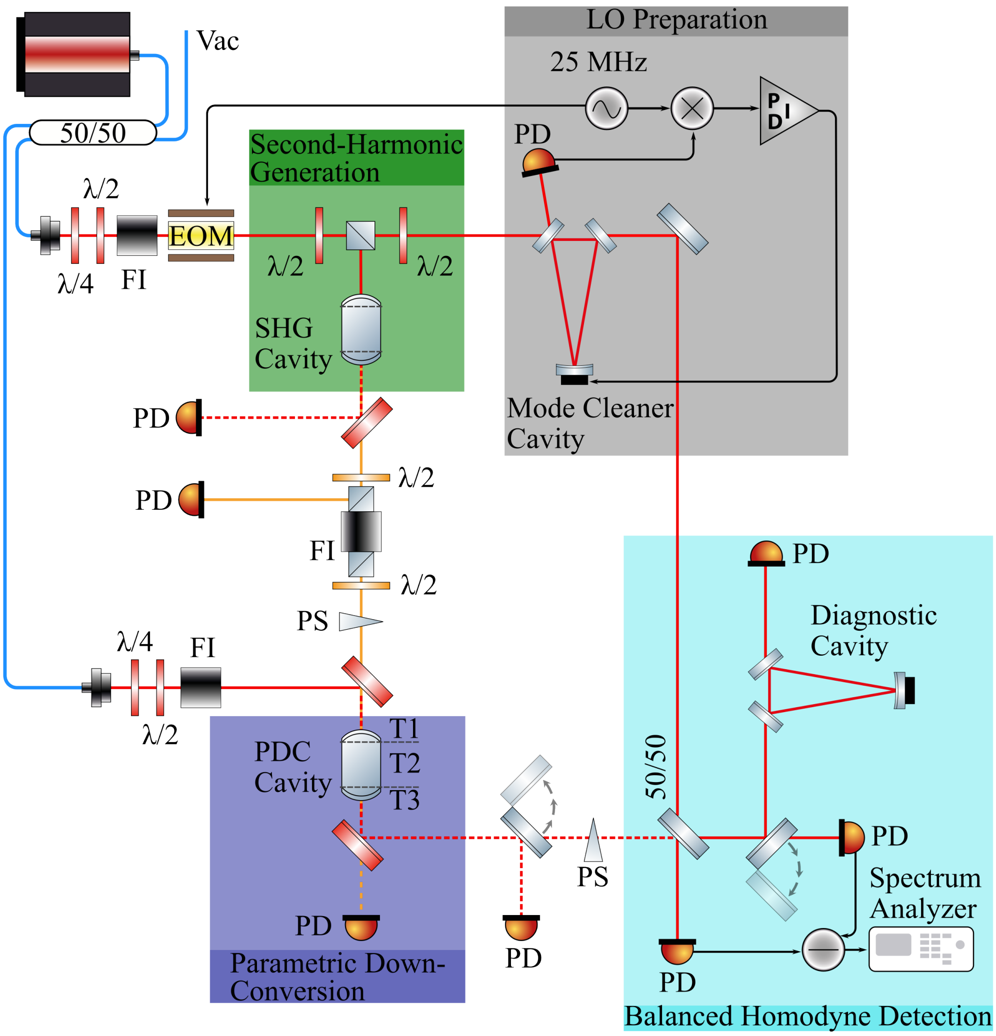

**Fig. 3.1: Schematic of the experiment's optical layout utilizing monolithic cavities.** The setup can be divided into different parts. The figure displays the second harmonic generation in green, which served as the pump for the PDC process highlighted in blue. The preparation for the local oscillator field is shown in the grey box. The squeezed states of light were detected and characterized using a balanced homodyne detection (light blue). EOM = Electro-Optic Modulator, FI = Faraday Isolator, PD = Photo Diode, PS = Phase Shifter, T1 = Temperature 1, T2 = Temperature 2, T3 = Temperature 3

## 3.1 Experimental setup

The experiment was set up on a breadboard with dimensions of 80 cm x 80 cm. A scheme of the experimental setup is depicted in fig 3.1 and is segmented into different parts highlighted by coloured boxes. The light source was a wavelength tunable NKT Basic + NKT Boostik fiber laser system operating at a wavelength of 1550 nm. A 50/50 fibre splitter divided the light in a signal and control beam path. A Faraday isolator was placed in each path to protect the laser from back reflections. The signal path was further divided by a polarizing beam splitter (PBS) and $\lambda/2$ waveplate combination into the second-harmonic generation (green) and local oscillator preparation (grey). In the local oscillator path, a ring cavity (mode cleaner) was used to filter out all non TEM00 modes. Utilizing the Pound-Drever-Hall control loop kept the mode cleaner on resonance. The required phase modulation side bands for this locking scheme were generated by an electro-optic modulator (EOM) at a frequency of 25.02 MHz. The SHG cavity provided the 775 nm light to pump the PDC process. A dichroic beam splitter filtered out the remaining 1550 nm pump light which could be used to monitor the conversion process. A portion of the converted light was reflected by a PBS for monitoring purposes. The squeezed vacuum was generated in the PDC cavity (blue) and a DBS directed it to the balanced homodyne detection (light blue). For the homodyne detection, the local oscillator and the squeezed vacuum were spatially overlapped on a 50/50 beam splitter. This was achieved by matching both beam paths onto a ring cavity (diagnostic cavity). In order to match the squeezed vacuum beam path, the control beam injected through the backside of the PDC cavity was needed.

### 3.1.1 Monolithic non-linear cavities

In this setup, a monolithic cavity design was used for the non-linear processes discussed in chapter 2. A 11.2 mm long ppKTP crystal was used as a non-linear medium. The crystal's end faces were curved with a radius of +10 mm and coated to form the cavity mirrors. For the SHG, the incoupling side featured a HR coating for 775 nm and an 82 % reflectivity coating for 1550 nm, while the backside was coated with high reflectivity for 1550 nm and 96 % for 775 nm. The PDC cavity was identical to the SHG, but the incoupling side and backside were switched. Those coatings led to a cavity linewidth of 226 MHz for 1550 nm and 123 MHz for 775 nm in both cavities.

A scheme of the cavity setup is depicted in figure 3.2. The crystal was placed on a heating pad with three Peltier elements underneath in order to separately heat (a) the center to hit the phase matching condition and (b) end faces to compensate

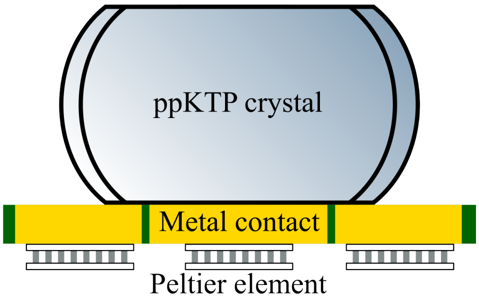

**Fig. 3.2: Schematic of the monolithic cavity.** The ppKTP crystal with curved and coated end faces laid on a heating pad with Peltier elements underneath to separately heat the center and end faces. Metal contacts ensured the heat conduction between Peltier elements and crystal. NTC elements, not shown in the graphic, monitored the temperatures.

for phase mismatches upon reflection, and to adjust the cavity length. These phase mismatches arose from the Gouy phase shift [LS07], the coating penetration depth, and the length of the last domain, which can be elongated or shortened depending on the crystal cut. In an optimal case, the last domain is cut exactly in half resulting in a normal domain length upon reflection. However, it was technically not possible to achieve this optimal case, since cutting the crystal underlays an error margin and the end faces were shortened by polishing them to obtain a curvature.

The heating pad is mounted on an aluminium frame, which additionally acted as a heat sink for the Peltier elements' cold sides. A PEEK element underneath the heating pad enclosed each Peltier element for a better separation of the temperature zones. A second PEEK element held the crystal in place on top of the heating pad. A POM enclosure was be placed on top to reduce air fluctuation. NTC elements were placed in close proximity to the Peltier elements to monitor the temperatures. With the NTC signal, the temperatures were kept stable to manually adjusted set points with a control loop actuating on the Peltier elements' currents.

### 3.1.2 Second harmonic generation in a monolithic cavity

In contrary to different cavity designs, the monolithic cavity length could not be actuated by a piezo-electric actuator. Therefore, to modematch light to the SHG cavity, the frequency of the master laser was modulated. With this method, a mode matching of 99 % was achieved. To determine the conversion efficiency, the converted power was measured behind a dichroic beamsplitter to prevent remaining 1550 nm light influencing the measurement. The power conversion was measured at different 1550 nm pump powers, and the corresponding efficiencies are shown in figure 3.3. A

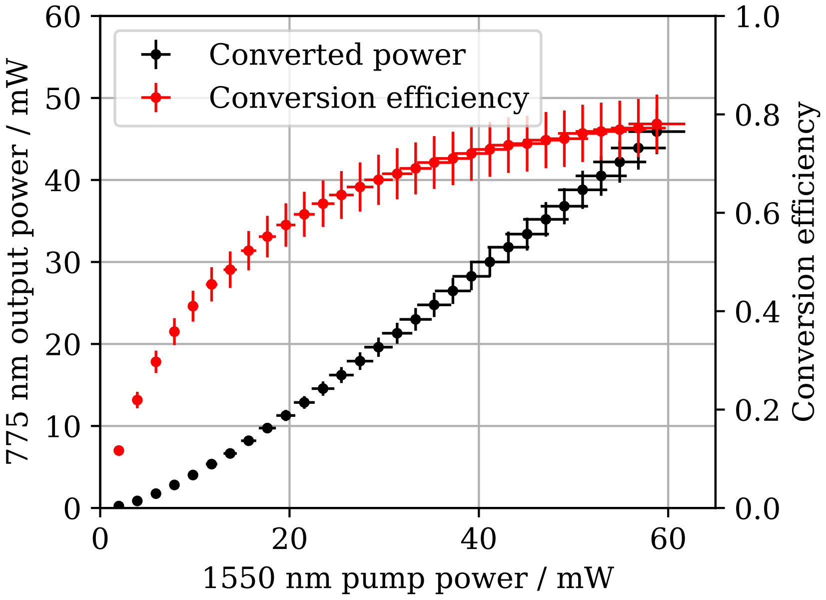

**Fig. 3.3: Conversion efficiency of the monolithic SHG cavity.** A conversion efficiency of about 77 % was achieved at an input power of approximately 60 mW. The converted light was measured behind a dichroic beam splitter. The powermeter had an error of 6 % for 775 nm and 5 % for 1550 nm.

maximum conversion efficiency of 77 % was observed at an input power of approximately 60 mW. It appeared that the global maximum of conversion efficiency could be found at higher pump powers. However, the converted power of approximately 46 mW at a pump of 60 mW was more than enough to pump the PDC, which oscillation threshold was expected to be below 30 mW.

Due to the aforementioned missing piezo electric element in the cavity design, a control loop acting on the cavity temperatures to keep the cavity length stable was required. At the time of the experiment, the control loop was not yet developed. However, the system could achieve a fairly stable conversion for a couple of minutes by allowing it to heat up and reach thermal equilibrium [Hag19, p.28-30]. Nevertheless, the system was highly sensitive to air fluctuations.

The efficiency measurement was done at a wavelength of 1550.1438 nm.

## 3.2 Squeezed states of light measurement in the MHz regime

The squeezed vacuum states generated in the PDC cavity were measured with a homodyne detector. Mandatory for the detector was a high dark noise clearance to observe large squeeze factors and a linear response. Formula 2.50 states that a doubling of the local oscillator power results in a noise power increase by the factor of two. Therefore, when measuring the vacuum noise, the noise power must increase by 3 dB after doubling the local oscillator power. Figure 3.4 shows the linearity of the used homodyne detector for local oscillator powers up to 32 mW. Small deviations from 3 dB were caused by the 5 % error of the power meter used for the determination of the light powers.

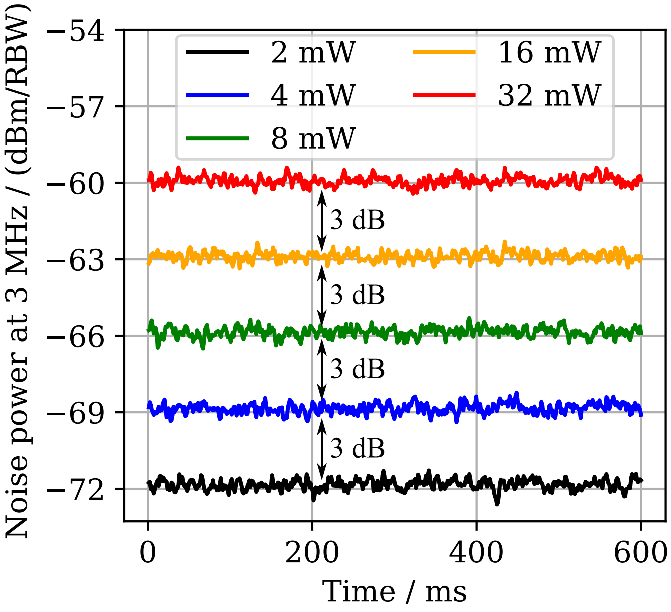

**Fig. 3.4: Linearity of homodyne detector at a Fourier frequency of 3 MHz.** Local oscillator powers were measured in the range of 2 mW to 32 mW. Doubling the power led to a 3 dB increase in the noise level, indicating the detector's linearity. The resolution bandwidth was set to 300 kHz, the video bandwidth to 300 Hz.

The squeeze factor was determined in a zero span measurement at a Fourier frequency of 3 MHz, which is shown in figure 3.5. The black trace depicts the vacuum noise with a clearance of $(22 \pm 0.1)$ dB to the dark noise (grey). Both lines were averaged over 5 traces by the spectrum analyser. Visible in the blue trace is the noise power of the squeezed quadrature with a squeeze factor of $(10.4 \pm 0.1)$ dB. The readout phase was adjusted manually at the phase shifter in the local oscillator path. Slowly shifting the local oscillator phase scanned the entire phase space between squeezed and anti-squeezed quadrature, depicted in the orange trace. The cavity resonances collapsed due to missing control loops for stabilizing the cavity lengths, before a trace for the corresponding anti-squeezed quadrature could be measured. However, an estimation of $(17.8 \pm 0.1)$ dB was taken from the phase scan. The corresponding optical loss was calculated to 7 %, which was mostly dominated by the spatial overlap of $V = 0.98$ leading to 4 % of loss and the photo diodes' quantum efficiency of $\eta = 0.99$ as stated by the manufacturer. Imperfect AR coatings of optics in the beam path and the escape efficiency of the PDC cavity caused the remaining 2 % of loss.

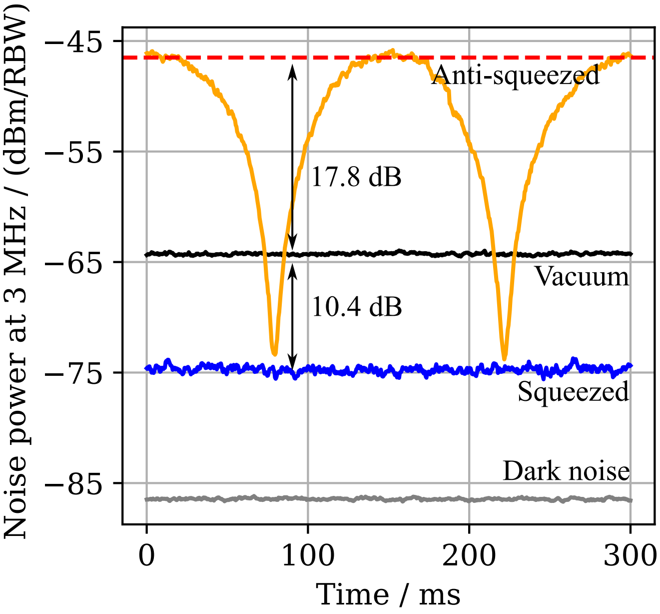

**Fig. 3.5: Zero span measurement at a Fourier frequency of 3 MHz.** The blue trace shows a squeezed vacuum state with a squeeze factor of $(10.4 \pm 0.1)$ dB. The corresponding anti-squeeze factor (red) was estimated to $(17.8 \pm 0.1)$ dB from the phase scan illustrated in the orange trace. The shot noise is depicted in the black trace. The resolution bandwidth was set to 100 kHz, the video bandwidth to 100 Hz.

To achieve this $(10.4 \pm 0.1)$ dB measurement, the PDC cavity was pumped with $P_{Pump} = 35\,\mathrm{mW}$, and the fundamental wavelength was tuned to 1550.081 nm for the PDC cavity to be double resonant. The cavity temperatures were set to 39.3°C for the phase matching, and at the end faces to 37.9°C and 30.8°C. As the tuned wavelength was not optimal for the SHG cavity, the conversion efficiency decreased. However, at a pump power of approximately $P_{pump,SHG} = 120\,\mathrm{mW}$ roughly 60 mW were converted to 775 nm, which provided sufficient pump power for the PDC cavity.

## 3.3 Double resonance in a monolithic cavity

As mentioned in the previous sections of this chapter, a double resonance could not be achieved for any given wavelength in the used monolithic cavity design. A further investigation with a qualitative simulation using the *Double Resonance Calculator* programmed by Maik Schröder is depicted in figure 3.6. These simulations show the resonance of a fundamental and a second harmonic field inside a cavity while varying two cavity parameters. The red traces indicate the fundamental wavelength of

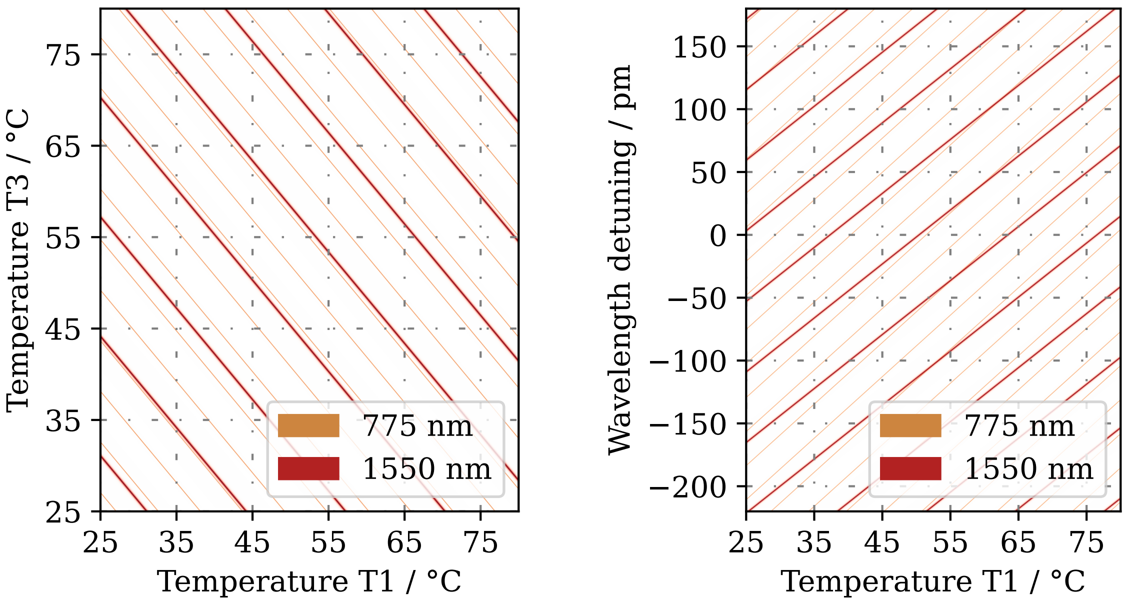

(a) By tuning the both edge temperature of the crystal, it is not possible to achieve a double resonance. The traces indicating the resonance of the cavity for the light fields run parallel. Thus an overlap between those might not be possible in the applicable temperature range.

(b) Detuning the fundamental wavelength leads to possible parameters enabling double resonance in a monolithic cavity.

**Fig. 3.6: Simulation of conversion parameters for a monolithic cavity.** These simulation show possible parameters to achieve a cavity resonance for a fundamental field and it's second harmonic. Here, 1550 nm are represented by the thick red lines and 775 nm by thin orange lines. When lines are crossing, the cavity is double resonant and a conversion is possible. One can see, by tuning only the edge temperatures a conversion is not necessarily possible for a given wavelength in a monolithic cavity. To achieve conversion, the fundamental wavelength must be detuned. The images were generated using the "Double resonance calculator" for python written by Maik Schröder.

1550 nm, while the orange traces indicate the second-harmonic 775 nm. Their thickness corresponds to the cavity linewidth for the fields.

A simulation of the cavity resonances while actuating the cavity's edge temperatures is shown in figure 3.6(a). The lines indicating the cavity's resonances run in parallel, making it uncertain to find a double resonance point within the Peltier elements' range for a fixed wavelength. However, the simulations do not provide a quantitative result due to deviations from the desired cavity parameters, such as coating reflectivities, length and end face curvatures, during the manufacturing process. A fortunate combination of these actual cavity parameters may result in two exactly overlapping lines and potential double resonance points can be found within the system's temperature ranges. Nevertheless, it cannot be predicted in advance and must be tested with the cavity itself.

Another effect observed in the simulation is the 1550 nm field's FSR being larger than two FSRs of the 775 nm field. This finding implies that adjusting only one edge temperature to jump from one resonance of the fundamental field to the next results in different distances to the nearest potential second-harmonic resonance. This effect can be explained by the FSR's dependence on the round trip length. Adjusting the edge temperatures results in different changes in the refractive indices $n_{1550\,\mathrm{nm}}, n_{775\,\mathrm{nm}}$ leading to a different optical path length inside the cavity.

The simulation in figure 3.6(b) studies the cavity resonances for a tuned fundamental wavelength and one actuated edge temperature. Crossings between the fundamental and second harmonic traces are clearly seen. Thus, for a given cavity, a double resonance can be found, if the fundamental wavelengths is slightly tuned. During the experiment it was observed, that the SHG and PDC cavities did not share the same detuning required to achieve optimal double resonance points. This effect is also a result of the error margins in the manufacturing process mentioned before.

In order to find a wavelength tuning with a double resonance point for the PDC cavity, the cavity could be used as an SHG, since it is the inverse process. Figure 3.7 shows a measurement of wavelength tunings with double resonance points for the SHG and PDC processes. For this measurement, the fundamental wavelength was modulated around an initially tuned fundamental wavelength point. The initial wavelength tuning was varied in 0.02 nm steps in the master laser's tuning range of 1549.92 nm to 1550.32 nm. In order to observe a maximum conversion signal on a photo detector, the cavity temperature were fine tuned for each measurement point. Wavelength tuning points with a local maximal conversion occurred in steps of either 60 pm or 80 pm. This is in good accordance with the simulation in figure 3.6(b). Here, the wavelength tunings with double resonant points occurred in steps in the range of 65 pm to 80 pm. It appeared in the measurement, that the wavelength of 1550.30 nm is the best operating point of the PDC cavity. However, a sufficient mode matching onto the 50/50 beam splitter for the homodyne detection wasn't achieved at this point. This indicates, that a higher order mode might have contributed to the second harmonic generation. Thus, the wavelength of 1550.081 nm was chosen to characterize the squeezed vacuum states.

## 3.4 Conclusion

The presented source of squeezed states of light was set up on a breadboard with the footprint of 80 cm x 80 cm and utilized double resonant monolithic cavities to

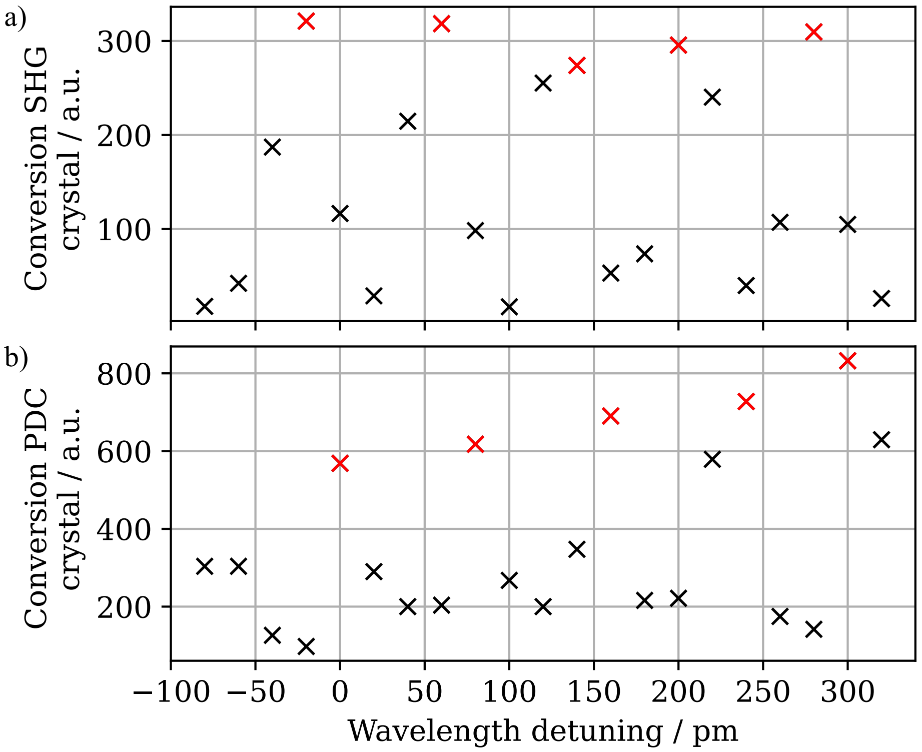

**Fig. 3.7: Wavelength tunings for double resonance points for the monolithic cavities** Both non-linear cavities were utilized to drive a SHG process in order to find conversion points. The wavelength was modulated around an initially tuned fundamental wavelength point. They were varied in 0.02 nm steps in the range of -100 pm to 320 pm referenced to 1550 nm. At every measurement point, the cavity temperatures were optimized to achieve the highest conversion signal measured by a photo diode. Wavelength points with a local maximal conversion were either 60 pm or 80 pm apart and are highlighted in red.

enhance the SHG and PDC processes. It provides squeezed states with a squeeze factor of up to $(10.4 \pm 0.1)$ dB at a side band frequency of 3 MHz. The corresponding anti-squeeze factor was estimated to $(17.8 \pm 0.1)$ dB, which equals to a loss of 7 %.

It was not possible to achieve an optimal double resonance inside the cavities only by tuning the cavity temperatures. In order to do so, the master laser's wavelength had to be tuned to specific values. These wavelength points depend on cavity parameters, such as reflectivities, crystal length, and end face curvatures, which underlay error margins during the manufacturing process. Thus, two different monolithic cavities do not necessarily operate properly for at the same tuning point. This makes monolithic cavities impracticable for experiments,which require a specific wavelength or where two sources for squeezed states of light have to operate at the same wavelength.

For a stable generation of squeezed states of light, control loops to maintain a stable cavity length were required. After the experiment was conducted, Oke Huhs developed a control loop acting on the cavity temperatures for the SHG to maintain a stable conversion [Huh21]. However, the technique was not transferable to the PDC cavity. Once both cavities are stabilized, the squeezed phase can be stabilized over an extended time period with e.g. the coherent control locking scheme.

# Chapter 4

# Generation of a squeezed vacuum with a hemilithic cavity

The generation of squeezed states of light in a hemilithic cavity design, consisting of a crystal and one additional mirror, is a state-of-the-art technique to achieve high squeeze factors. Both current world records of measured squeeze factors for 1064 nm [VMC$^+$08] and 1550 nm [MWV22] were measured utilizing a hemilithic cavity-enhanced PDC process. The research of Axel Schönbeck also demonstrated the capability of using this cavity design for compact squeezed states of light sources [Sch18] and the setup presented in this experiment is based on his work and the improvements he made to the hemilithic cavity design.
Furthermore, this study investigates the design's tuning capabilities at the wavelength of 1550 nm, while generating high squeeze factors. Wavelength tunable sources have only been developed for optical wavelength ranges of $(855 \pm 0.005)$ nm [PCK92], $(836 \pm 5)$ nm [FWS$^+$93], $(472 \pm 4)$ nm [KCL21], and $(389.5 \pm 0.5)$ nm [BRF97]. However, none of these experiments generated squeeze factors beyond 5 dB.

## 4.1 Setup

The experimental setup was similar to the previously described one in chapter 3. Figure 4.1 depicts a scheme with highlighted parts in coloured boxes. As before, the SHG is shown in a green box, the PDC in blue and the on-board homodyne detection in light blue. However, some changes were made to make the source of squeezed states of light more compact and applicable for future experiments. For this experiment to fit on a breadboard with a footprint of 60 cm x 40 cm, the mode cleaner for the local oscillator was omitted from the setup. The NKT Basic + NKT Boostik fibre laser system providing the light for this experiment already had a very

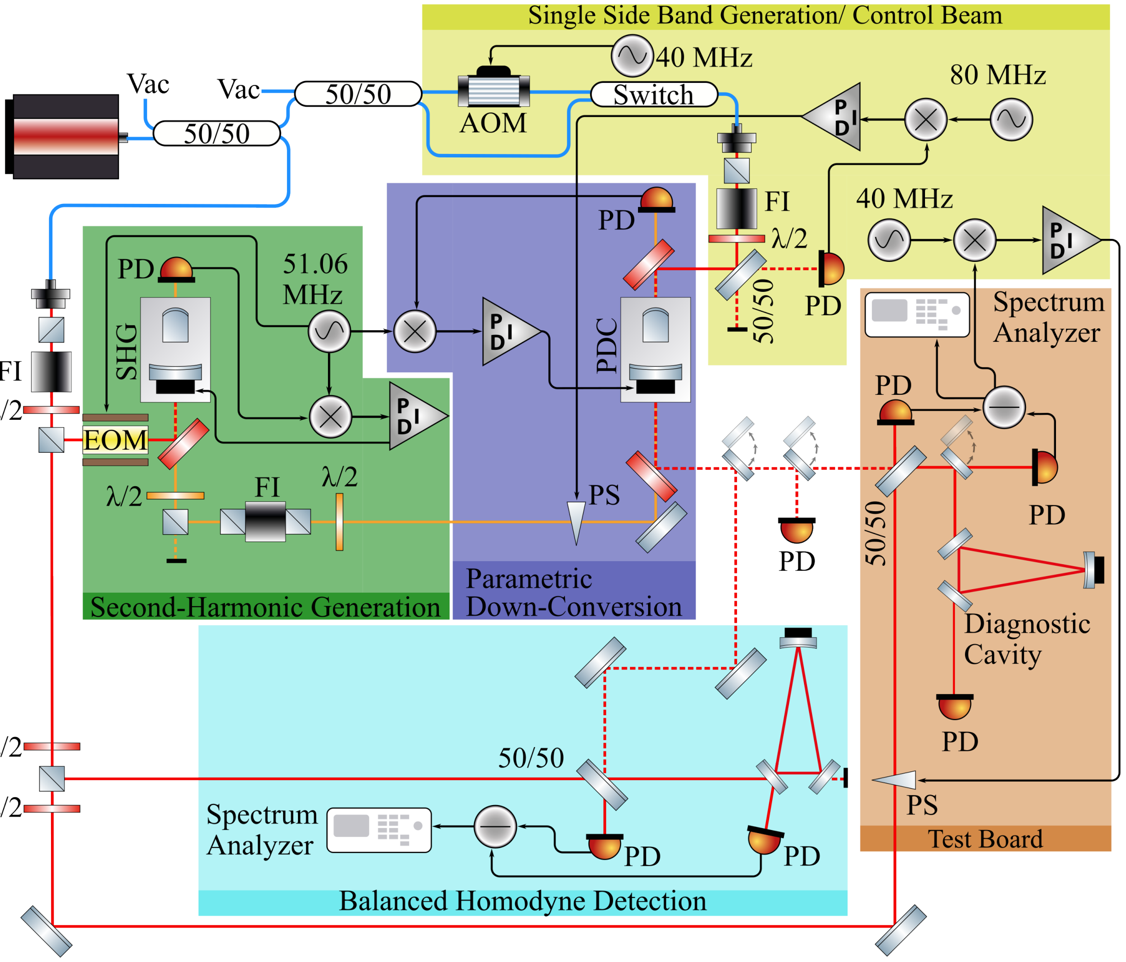

**Fig. 4.1: Schematic of the experiment's optical layout utilizing hemilithic cavities.** The setup is divided into different parts similar to the monolithic setup depicted in figure 3.1. The SHG generation, the PDC, and the homodyne detection are shown in the same colours as before. Additional to the on board homodyne detection, there is a second detection setup on an external *testboard* (orange). In yellow, the single sideband generation is shown. AOM = Acousto-Optic Modulator, EOM = Electro-Optic Modulator, FI = Faraday Isolator, PD = Photo Diode, PS = Phase Shifter

good spatial beam shape of the quality factor $M^2 < 1.05$. Further, the diagnostic cavity, to match local oscillator and signal beam path onto the 50/50 splitter, acted additionally as a mirror onto one of the homodyne detector's photo diodes. This was possible since the cavity reflected all incoming light as long as it was not resonant. Also the phaseshifter in the local oscillator path to adjust the readout angle was removed. An experiment, where a squeezed vacuum is provided by this source, has to implement a phase shifter for a controlled read out. To stabilize the phase of the squeezed vacuum, a coherent control scheme (shown in yellow) was implemented. How this control scheme works, will be explained later in this chapter. However, a single side band is mandatory for the coherent control scheme and was generated by a fibre-coupled acousto-optic modulator (AOM) at $f = 40\,\mathrm{MHz}$. To analyze the locking scheme, a second homodyne detection with a phase shifter in the local oscillator path was built on a second breadboard, shown in the orange box. A fibre switch ensured the possibility to switch between the single side band or a control beam to be injected through the backside into the PDC cavity. The cavity lengths of the SHG and PDC cavities were kept stable with the Pound-Drever-Hall locking scheme. An EOM in front of the SHG cavity provided the necessary side bands at a frequency of 51.06 MHz. Both cavities were locked using the second-harmonic field in transmission.

### 4.1.1 Hemilithic cavity design

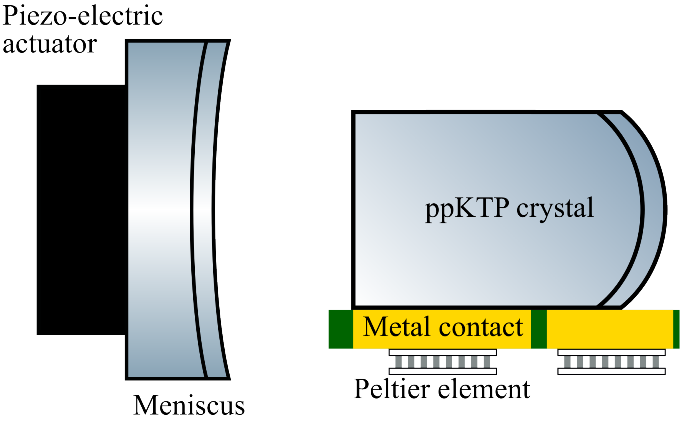

**Fig. 4.2: Scheme of the hemilithic cavity.** The crystal lays on a heating pad with two Peltier and NTC elements underneath to control the temperature of the crystal's center and end face. The incoupling mirror can be actuated with a piezo-electric element for cavity length control.

In comparison to the previously discussed monolithic cavity design, the crystal in the hemilithic design was curved with a 12 mm radius and HR coated on only one end face. The light couples into the cavity through an incoupling mirror. The incoupling mirror was a meniscus with a radius of curvature of 25 mm and reflectivities of 83 % for 1550 nm, 97.5 % for 775 nm. These reflectivities resulted in a cavity linewidth of 108 MHz for 1550 nm and 15 MHz for 775 nm. The incoupling mirror and crystal were spaced by a 24 mm air gap.

The mechanical design was similar to the one used in [Sch18, pp. 39-43]. A scheme is depicted in figure 4.2. Here, the cavity consisted of one aluminium frame holding the coupling mirror and a second base frame holding the non-linear crystal. Similar to the monolithic design, the crystal was placed on a heating pad with Peltier elements underneath, to control the temperatures of the crystal's center and coated end face separately. Thus, by heating the center, the phase matching condition was accomplished and heating the crystal's end face compensated for reflection phase mismatches. NTC elements next to the Peltier elements were used to monitor the temperature and keeping them stable to manually adjusted set points with a control loop. A PEEK element was placed on top of the crystal and screwed to the base ensuring the crystal alignment along the optical axis. A POM enclosure could be placed on top to shield the crystal from air fluctuations and dust.

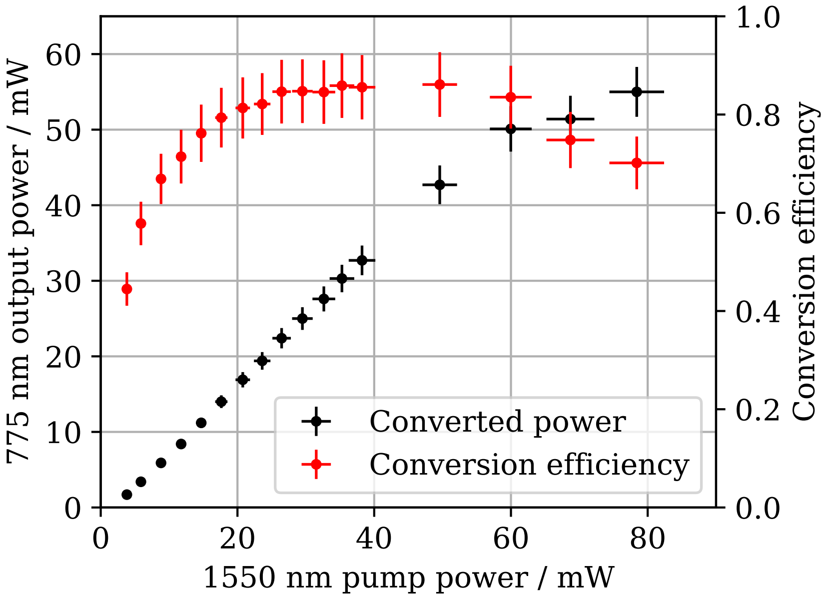

**Fig. 4.3: Conversion efficiency of the hemilithic SHG cavity.** With the hemilithic SHG a conversion efficiency of 86 % was achieved at a pump power of roughly 50 mW. The converted light was measured behind a dichroic beam splitter. The power meter had an error of 6 % for 775nm and 5 % for 1550 nm.

The meniscus was positioned on a piezo-electric element that allowed for control over the cavity length by pushing on the mirror. A brass ring kept the piezo-electric element in position and ensured the meniscus' center to be on axis with the frame. The position of both were fixed with a cover plate.

To align the frame holding the meniscus with the crystal axis, a laser beam was coupled into the cavity through the meniscus and the light transmitted through the back side of the crystal was detected with a photo diode. While scanning the cavity length by actuating the piezo-electric element, the Aluminium frame was slightly moved until a position was found, where cavity modes were observed on the photo diode. Screwing the aluminium frame to the base completed the cavity setup.

### 4.1.2 Second-harmonic generation

The SHG cavity's performance was characterized by measuring the converted power behind two dichroic beam splitters with a photo diode for increasing 1550 nm pump powers. Figure 4.3 shows this measurement. At an internal pump power of roughly 50 mW, a maximum conversion efficiency of 86 % was observed, which is lower than previously achieved conversion efficiencies of up to 95 % in a hemilithic cavity design [ANS+11]. However, the SHG cavity provided enough pump power for the PDC process, since the oscillation threshold was simulated to be in the order of $P_{thr} = 20\,\mathrm{mW}$.

## 4.2 Measurement in the MHz regime

For measuring the squeezed states of light, the homodyne detector presented in the previous section could not be used, since it wasn't equipped for the coherent control locking scheme. Thus, the linearity of this experiment's detector had to be determined as well. The corresponding measurement is presented in figure 4.4. The detector was linear for local oscillator powers up to 16 mW. For this measurement, the resolution bandwidth was set to 300 kHz for all traces, and the video bandwidth was set to 300 Hz. These settings were consistently employed for all measurements throughout this chapter.

Figure 4.5 shows the best zero span measurement obtained in this experiment. A squeezed vacuum state with a squeeze factor of (11.0 ± 0.1) dB (blue trace) was generated at a pump power of $P_{pump} = 15.2\,\mathrm{mW}$. The corresponding anti-squeeze factor was (19.8±0.1) dB above the vacuum noise (red trace), resulting in an estimated loss of 6.4 %. The visibility of $V = 98.3\,\%$ and the photo diodes' quantum efficiency of $\eta_{PD} = 99\,\%$ contributed the most to the optical loss. The remaining approximately

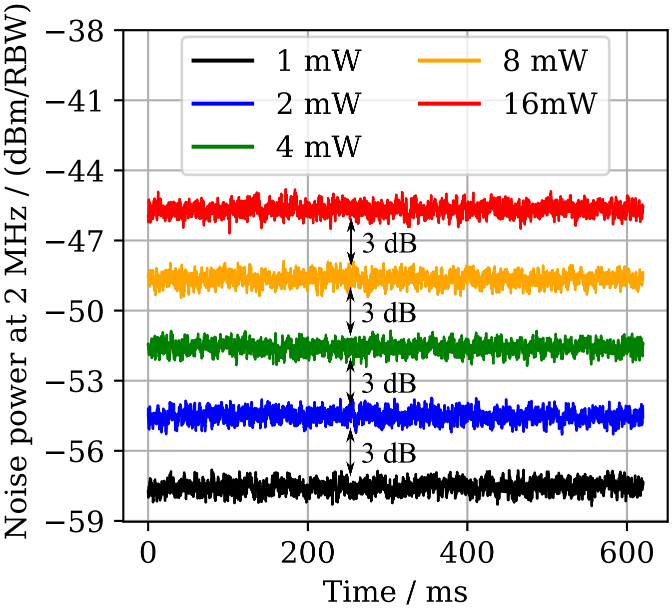

**Fig. 4.4: Linearity of the homodyne detector at a Fourier frequency of 2 MHz.** Vacuum noise levels were measured for local oscillator powers from 1 mW to 16 mW. Doubling the power resulted in a 3 dB increase of the noise level, indicating the linearity of the detector. The resolution bandwidth was set to 300 kHz, the video bandwidth to 300 Hz.

2 % of loss were composed of the escape efficiency and the AR coatings along the optical path. At a local oscillator power of 5 mW, the dark noise was $(22.3 \pm 0.1)$ dB below the vacuum noise and was not subtracted from the measurement. A scan over the phase space between squeezed and anti-squeezed quadrature was obtained by slowly shifting the pump phase (orange trace). For recording the squeeze and anti-squeeze quadrature, the pump phase was manually adjusted with a phase shifter. Cavity temperatures were optimized to a phase matching temperature of 40°C and an end face temperature of 32°C. Changing these cavity temperatures led to lower squeeze factors.

In addition to a zero span measurement at 2 MHz, where the homodyne detector exhibited the largest dark noise clearance towards the vacuum noise, the squeezed vacuum generation was characterized in a range from 1 MHz to 50 MHz. Figure 4.6 presents spectra for squeeze and anti-squeeze factors referenced to the vacuum noise. In this measurement, the dark noise shows two large peaks at 40 MHz and 50 MHz, where it was not possible to measure squeezed vacuum states. The first peak originates from parasitic effects of the electronics in the homodyne detector, while the second is exactly the phase modulation frequency of the PDC cavity's Pound-Drever-Hall control loop for the length stabilization. However, a squeeze factor of approximately 5 dB was still measurable at 50 MHz. From fits to the spectra

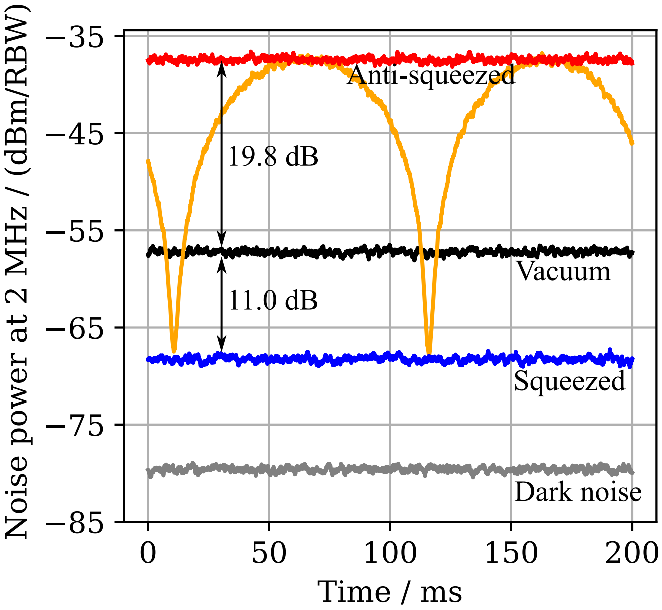

**Fig. 4.5: Zerospan measurement at a Fourier frequency of 2 MHz.** In blue, a squeezed vacuum state with a squeeze factor of $(11.0 \pm 0.1)$ dB with respect to the vacuum noise in black can be seen. The corresponding anti-squeezed vacuum state with an anti-squeeze factor of $(19.8 \pm 0.1)$ dB is shown in red. The dark noise was $22.3 \pm 0.1)$ dB below the vacuum noise. The resolution bandwidth was set to 300 kHz, the video bandwidth to 300 Hz.

according to equation 2.40, the linewidth was determined to 107 MHz, which is in good agreement with the simulated 108 MHz. To achieve higher squeeze factors at larger frequencies, the cavity must be designed with a larger bandwidth for 1550 nm.

## 4.3 Wavelength tunability of the squeezed vacuum states

A DRC simulation for the hemilithic cavity design is depicted in figure 4.7, where the crystal's end face temperature and the air gap were varied. The simulation gave the suggestion to find a double resonance point for any fundamental wavelength detuning. This would allow for the observation of squeeze vacuum states for any detuning in the experiment. Figure 4.8(a) displays a measurement confirming the tunability of the hemilithic cavity system. The temperature adjustments for the PDC cavity and observed squeeze factors are presented for different wavelengths. To adjust the wavelength, the master laser's wavelength was detuned in 0.02 nm steps from -0.1 nm to 0.34 nm, using 1550 nm as a reference. After adjusting the wavelength, a subsequent frequency stabilization time of at least 20 minutes followed. The sta-

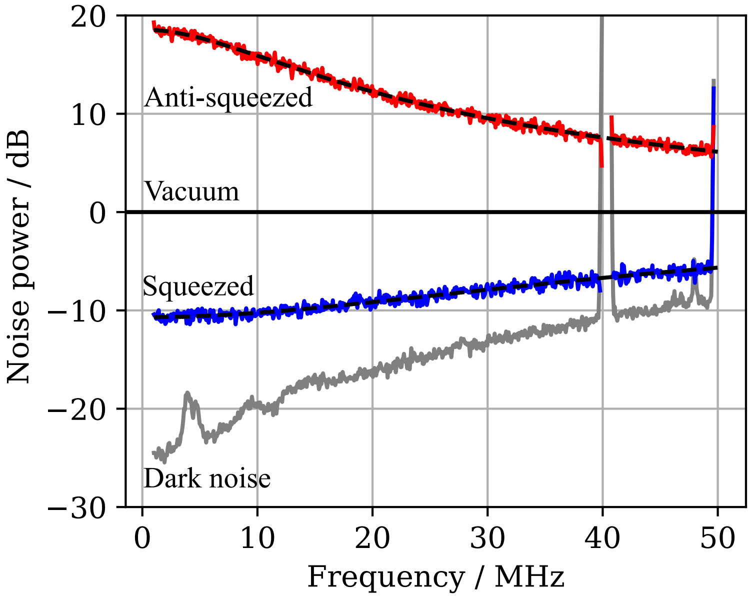

**Fig. 4.6: Squectra for squeeze and anti-squeeze factors normalized to the vacuum noise.** In blue, the spectrum for the squeeze factors are shown, while the one for anti-squeeze factors is depicted in red for a frequency range of 1 MHz to 50 MHZ. The grey trace shows the dark noise, which exhibited two peaks, where squeeze factors could not be measured. The PDC cavity's Pound-Drever-Hall length stabilization caused a peak around 50 MHz due to phase modulation. The peak at around 40 MHz is caused by parasitic effects in the homodyne detector's electronics. It is still possible to observe a noise reduction of approximately 5 dB at 50 MHz.

bilization time could not be avoided, because the master laser itself fine-tuned the output wavelength thermally. At each step, the phase matching and crystal end face temperature were manually adjusted and a zero span measurement was taken at a pump power of $P_{Pump} = 15.2\,\mathrm{mW}$ to determine the squeeze factors. All squeeze factors were $>(10.5 \pm 0.1)$ dB with an average of $(10.8 \pm 0.1)$ dB. Since the optical loss remained stable with a mean value of $6.5 \pm 0.1\,\%$, the fluctuations in squeeze and anti-squeeze factors were a result of varying internal pump powers of the PDC cavity. The observed differences in the results may be attributed to variations in the mode matchings onto the PDC cavity, which were caused by the measurements being taken over a period of four workdays and fluctuations in laser power. The fluctuations could be seen more clearly in the anti-squeeze factors, as the squeeze factors were more dominated by the overall optical loss.

The optimized temperatures in the crystal's center and end face showed a non-monotonic behaviour. This was unexpected, since the $dn/dT$ value of KTP doesn't change signs. A quasi phase matched system requires an elongated domain length at increased wavelengths. In this system, the domain length is controlled by heating

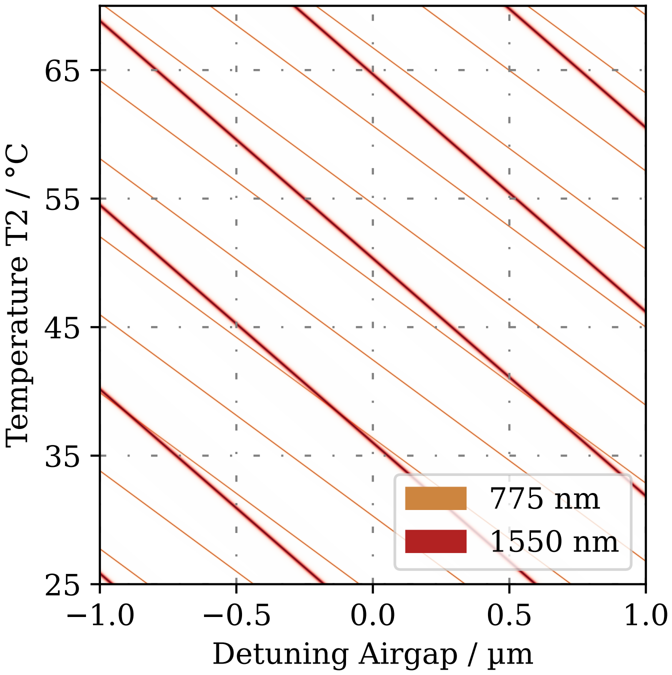

**Fig. 4.7: Simulation of conversion parameters for a hemilithic cavity.** A simulation similar to 3.6 for a hemilithic cavity suggests to find conversion points for an arbitrary wavelength due to the tunability the airgap and crystal end face temperature.

the crystal to change it's refractive index. Thus, it was expected that the phase matching temperature would increase with the wavelength. However, the compact cavity design could cause this behaviour. The two temperature regions were not entirely decoupled from each other and the NTC sensors were affected by both Peltier elements.

A similar measurement shown in figure 4.8(b), where only the phase matching temperature was adjusted after tuning the wavelength, emphasised the latter point. The crystal's center temperature showed a monotonous behaviour with an increase in wavelength after tuning, while the side temperature increased due to thermal coupling and the heating power of the center Peltier element. To achieve comparable squeeze factor compared to the two fine tuning temperature case, the pump power had to be increased. Here, the pump power was $P_{Pump} = 15.8\,\mathrm{mW}$ to generate squeeze factors $>(10.5 \pm 0.1)\,\mathrm{dB}$ with an average of $10.7 \pm 0.1\,\mathrm{dB}$, which corresponds light power increase of $4\,\%$. This relative small difference in pump power might be a result of using a crystal with a fortunate combination of crystal cut and phase pick up upon reflection at the end face. Both factors can't be predicted or determined beforehand, since they occur randomly in the manufacturing process.

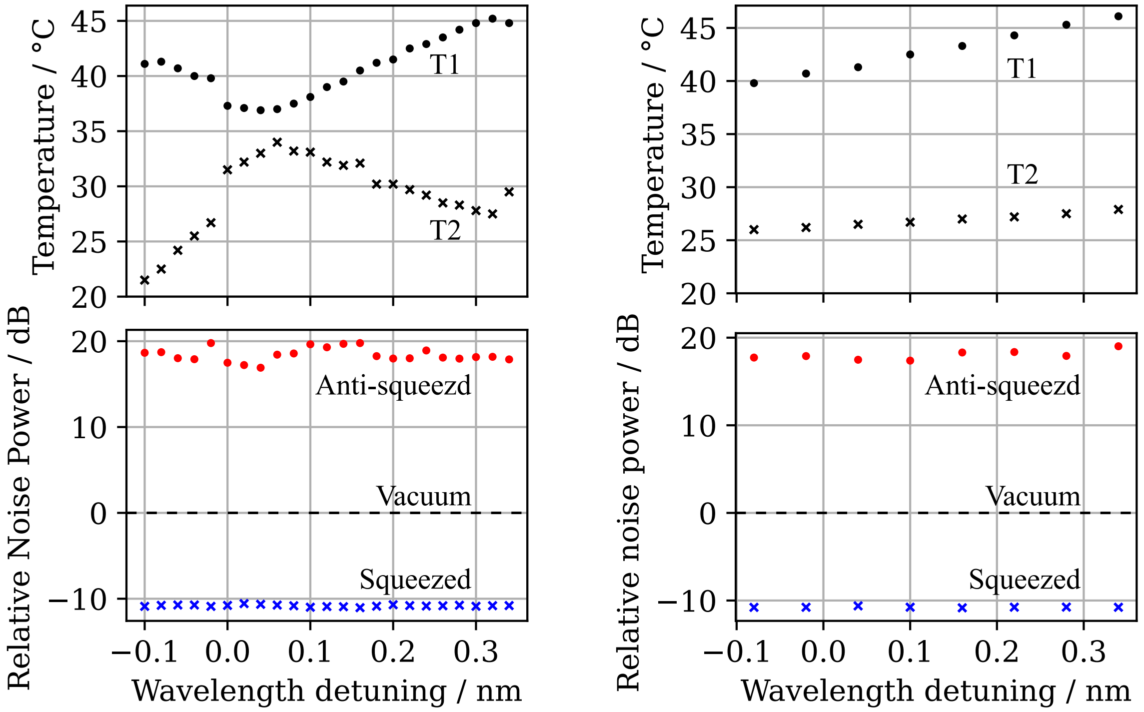

(a) Perfomance of PDC cavity at detuned wavelength with two actively controlled crystal temperatures.

(b) Perfomance of PDC cavity at detuned wavelength with actively controlled phase matching temperatures. The crystal end face only heated up due to the phase matching temperature.

**Fig. 4.8: Crystal temperatures and squeeze factors at detuned wavelengths.** Zero span measurements were taken at detunings ranging from -0.1 nm to 0.34 nm around the central wavelength of 1550 nm. In (a), phase matching (T1) and crystal end face (T2) temperature were adjusted for each detuning. All squeeze factors were $>(10.5 \pm 0.1)$ dB with an average of $(10.8 \pm 0.1)$ dB at a pump power of $P_{Pump} = (15.2 \pm 0.7)$ mW. Only adjusting the phase matching temperature in (b) yielded comparable squeeze factors $>(10.5 \pm 0.1)$ dB at an increased pump power of $P_{pump} = (15.8 \pm 0.7)$ mW.

For the SHG cavity, an improvement due to the two adjustment temperatures could not be observed. Figure 4.9 displays the fine-tuning temperature during the measurements in 4.8. In these two measurements with the same wavelength changes, a non-monotonic and a linear behaviour of the temperature curve was observed. The insensitivity to certain temperature set points compared to the PDC cavity might be explained by larger cavity linewidth for the 1550 nm field compared to the 775 nm field. Upon conversion, intra-cavity loss was induced for the fundamental field resulting in a further increase of the 1550 nm cavity linewidth. The gradient around the resonance peak flattens, which increased the region with similar conversion around the center. Thus, the margin for the temperature adjustment where the fundamental and second harmonic fields overlap might be increased. It would have to be checked

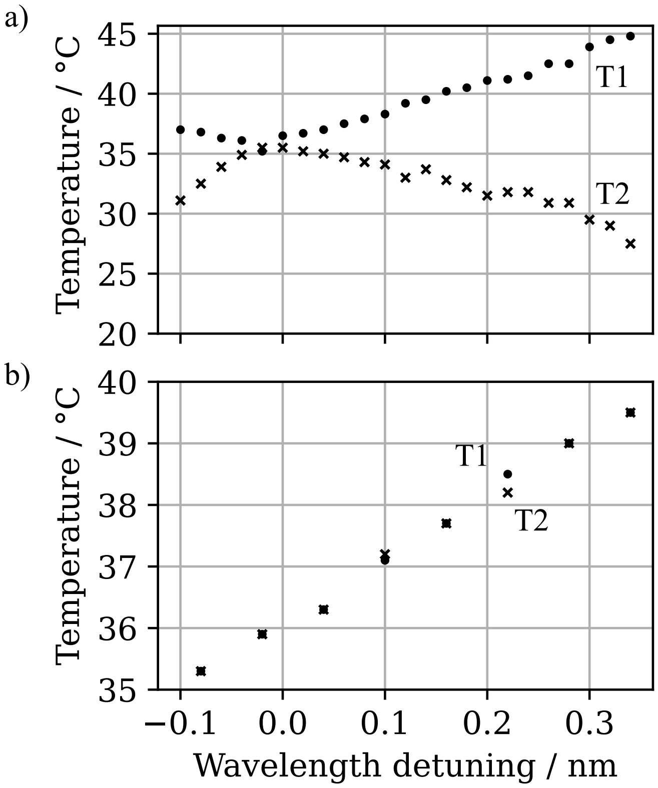

**Fig. 4.9: SHG crystal temperatures for detuned wavelengths.** For tunings in the range of -0.1 nm to 0.34 nm, the SHG crystal is less sensitive to temperature adjustments. The SHG cavity temperature adjustments in the top graph corresponds to the measurement in figure 4.8(a) and the adjustments in the bottom graph corresponds to the measurement in 4.8(b). A large gap or same values for phase matching (T1) and crystal end face (T2) temperatures at a given wavelength did not affect the conversion efficiency.

whether the effect occurs in the PDC cavity if the linewidth of the second-harmonic pump field is significantly larger than that of the fundamental field.

However, the comparison between the temperature curves for PDC and SHG might not be possible, as the dynamics between the cavity-enhanced SHG and PDC process differ. Nevertheless, further experiments would be necessary to gain more insights into this behaviour of the systems.

The wavelength range of the source of squeezed states of light was limited by the range of the used master laser. A lower limit for the temperatures were set to room temperature (20° C) to avoid water condensation inside the cavity. A temperature upper limit was given by the maximum heating power of the Peltier elements at 70° C.

A paper covering the results presented in this section is published in Optics Express under the title *A 10-dB squeeze laser tuneable over half a nanometer around 1550 nm* [HZSS24].

## 4.4 Long term stability

For a Squeeze Laser to be used in further experiments, the squeeze ellipse needs to be stable over a long time period. In this setup, the coherent control locking scheme is utilized for this purpose.

### 4.4.1 Coherent control control loop

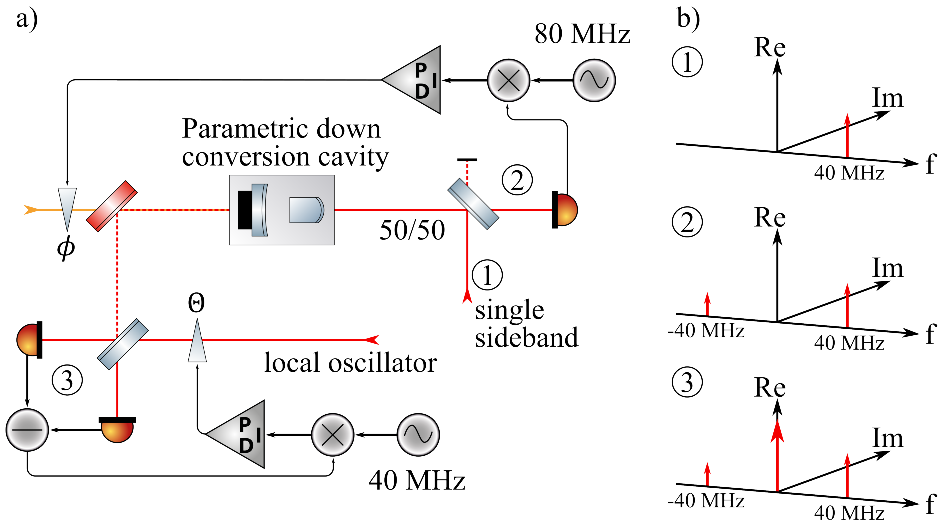

**Fig. 4.10: Schematic of the coherent control locking scheme.** The single side band generated by a fibre based acousto-optic modulator at a frequency of 40 MHz is injected through the high reflective backside into the PDC cavity. The side band seeds a PDC process generating a second side band. The beating signal of those side bands leaving through the backside is picked up by a photo diode behind a 50/50 beamsplitter. With the homodyne detector, the beating signal between local oscillator and side bands is detected. The diagrams on the right are phasor pictures for the corresponding positions 1, 2 and 3 in the schematic on the left.

The coherent control method was developed for stabilizing squeezed states in the audio frequencies and was successfully tested in the gravitational wave detector GEO600 [GDD+13] [KVL+12]. A brief description will be represented here, with detailed informations available in [CVDS07] [Che07, pp. 161 ff.] [Vah08, pp. 71 ff.]. Figure 4.10 illustrates the coherent control scheme with phasor diagrams and its integration in the setup. In order to actively control the squeeze angle and homodyne readout angle with respect to each other, it is crucial to create an interaction, which establishes a phase relationship between those angles. Here this relationship is established by a single side band interacting with the crystal in the parametric down-conversion cavity. The single side band is generated by a fibre-based acousto-optic modulator at a frequency of 40 MHz. It is injected through the high reflective backside of the PDC cavity, where it seeds a parametric down-conversion process. Thus, a second side band is created at a frequency of -40 MHz. The electric field leaving the cavity is proportional to

$$E_{out}(t) \propto \frac{1+g}{\sqrt{2g}}\alpha_\Omega \cos(\nu + \Omega t) - \frac{1-g}{\sqrt{2g}}\alpha_\Omega \cos(\nu t - \Omega t - 2\phi). \tag{4.1}$$

In this expression is $g = e^{2r}$ with the squeeze factor $r$ and $\phi$ being the squeezing phase, which is directly related to the 775 nm pump field. $\alpha_\Omega$ denotes the amplitude of the side band. The electric field is detected with a photo diode behind a 50/50 beam splitter. Thus, the photo current is proportional to the intensity

$$I_{out} = |E_{Out}|^2 \propto \frac{\alpha_\Omega^2}{2g}[(1+g)\cos(\nu + \Omega t) - (1-g)\cos(\nu t - \Omega t - 2\phi)]^2, \tag{4.2}$$

which is modulated by a beating between the side bands. Since both side bands are shifted by 40 MHz away from the carrier, a demodulation frequency of $2\Omega = 80$ MHz has to be chosen to obtain an error signal. Choosing a suitable demodulation phase, the error signal can be written as

$$\epsilon_{pump-phase} \propto \frac{\alpha_\Omega^2(g^2-1)\sin(2\phi)}{4g} \tag{4.3}$$

This error signal depends on the squeezing angle $\phi$ with respect to the side band. In the experiment, the error signal was fed back to a phase shifter in the pump field to stabilize the pump phase and thus the squeeze state's phase.

As a second step, an error signal for the homodyne readout angle has to be obtained. It is derived from the beating between the local oscillator and the side bands coming out of the PDC cavity. The electric fields on the homodyne detector's photo diodes are given by

$$\begin{aligned} E_{PD1} \propto \frac{1}{\sqrt{2}}\Big[\alpha_{LO}e^{-i(\nu t+\Theta)} + \Big(\frac{1+g}{\sqrt{2g}}\alpha_\Omega \cos(\nu t + \Omega t) \\ -\frac{1-g}{\sqrt{2g}}\alpha_\Omega \cos(\nu t - \Omega t - 2\phi)\Big)\Big] + c.c. \end{aligned} \tag{4.4}$$

and

$$E_{PD2} \propto \frac{1}{\sqrt{2}}\Big[\alpha_{LO} e^{-i(\nu t+\Theta)} - \Big(\frac{1+g}{\sqrt{2g}}\alpha_\Omega \cos(\nu t + \Omega t) - \frac{1-g}{\sqrt{2g}}\alpha_\Omega \cos(\nu t - \Omega t - 2\phi)\Big)\Big] + c.c. \tag{4.5}$$

The homodyne detector subtracts the photo currents, resulting in

$$I_{diff} = \frac{2\sqrt{2}\alpha_{LO}\alpha_\Omega(-1+g)}{\sqrt{g}} \cos(\Omega t + 2\phi + \Theta). \tag{4.6}$$

$\Theta$ denotes the phase between pump and local oscillator. Thus, a demodulation with the frequency $\Omega$ results in an error signal for the readout angle

$$\epsilon_{homodyne} = \frac{2\sqrt{2}\alpha_{LO}\alpha_\Omega(-1+g)}{\sqrt{g}} \sin(2\phi + \Theta). \tag{4.7}$$

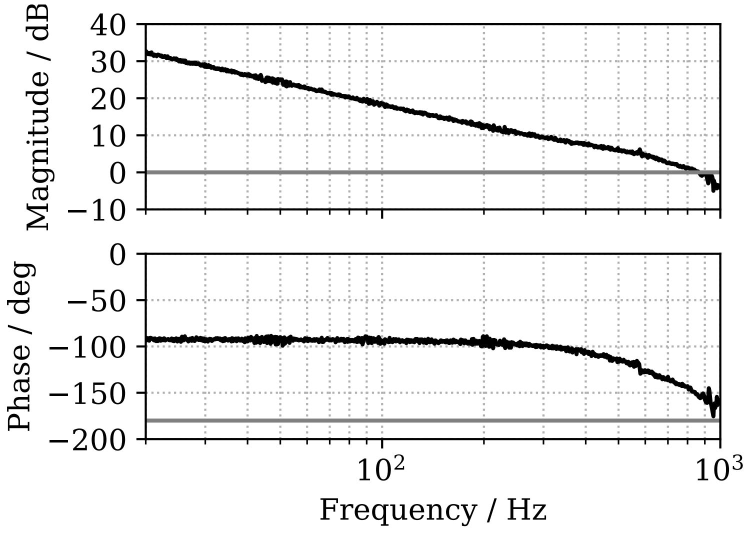

**Fig. 4.11: Open loop measurement of the pump field phase stabilisation.** A unity gain of roughly 850 Hz was achieved for the control loop stabilizing the pump field phase. For the stabilization of the local oscillator phase not shown here, a similar bandwidth was achieved.

This error signal also depends on the squeezing angle $\phi$. As shown above, the squeezing angle can be stabilized independently. With a constant $\phi$, the stable phase relation between squeezing and readout angle can be established. In the experiment, $\epsilon_{homodyne}$ is fed back to a phase shifter in the local oscillator path.

Figure 4.11 shows exemplary the signal response of the control loop stabilizing the pump field phase. The unity gain marking the bandwidth was around 850 Hz. The PID controller of the local oscillator control loop for frequency shaping was build the same and its signal response showed a similar behaviour with a similar unity gain around 850 Hz.

### 4.4.2 Long term stability measurement

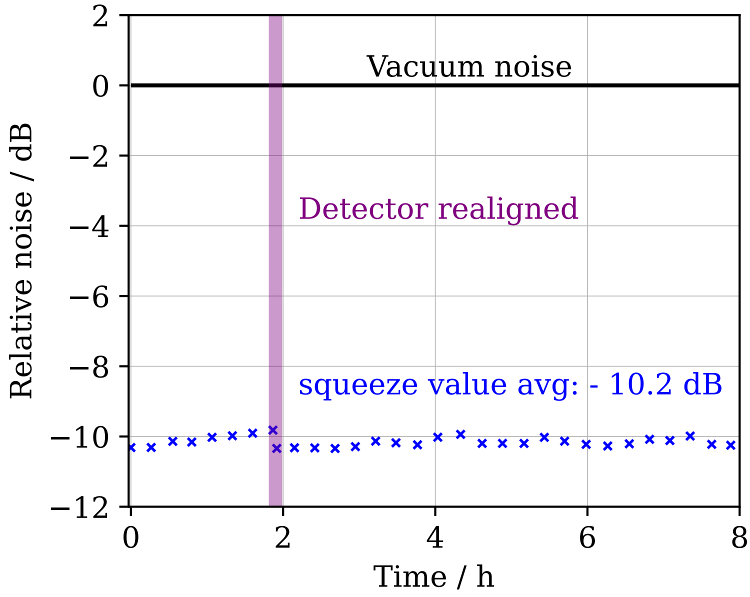

**Fig. 4.12: Stability of the squeezed light source over 8 hours.** Squeeze factors were measured with a zero span measurement every 15 minutes over a time period of 8 hours. After 2 hours, the control loops of the coherent control scheme needed to be realigned to prevent the system from drifting further below 10 dB. Over the whole time period, the squeeze factor was $(10.2 \pm 0.1)$ dB on average.

To maintain a stable squeezed vacuum state over an extended time period, it was crucial to avoid large phase drifts between the light fields for signal and single side band generation, besides thoroughly adjusted electronics for the control loops. As shown in figure 4.1, several fibre optics were used to separate the signal generation from the single side band generation. Hence, both light fields could experience different phase drifts inside the fibres due to thermal fluctuations. If the phase drift between the fields was too large, the range of the piezo-electric actuators could not compensate for it and the control loops failed. By housing the fibres in foam material, they were isolated from surrounding air fluctuations, circumventing this problem.

Phase drifts in the fibre affected p and s polarisation differently. This means that the ratio of p-polarised light to s-polarised light remained constant, while the phase between the two altered. In combination with waveplates and a Faraday isolator after coupling the light out of the fibre, it created a power fluctuation causing instabilities in the error signal for the squeezed state's phase stabilisation. By using polarisation beam splitters directly behind the fibre (out-) couplers, the polarisation maintained stable in front of the Faraday isolator, resulting in a stable intensity and a stable error signal.

With those improvements to the system, The coherent control locking scheme enabled the generation of a stable squeezed vacuum for 8 hours. The measurement is shown in figure 4.12. A zero span measurement was taken every 15 minutes to determine the squeeze factor. On average, a squeeze factor of $(10.2 \pm 0.1)\,\mathrm{dB}$ was measured over the 8 hour time span. The purple line indicates a point after approximately 2 hours, where the system drifted below 10 dB. To counteract this behaviour, the control loops for the coherent control scheme were relocked. This did not need to be repeated again for the remaining measurement.

Overall, this measurement demonstrates the potential of the system to be applicable in further experiments. In fact, the presented squeezed states of light source was brought to the ETH Zürich in Switzerland, after an automatic locking scheme with further improvements to the electronics to operate the system was implemented by Dr. Jan Südbeck, Dr. Jascha Zander and Dr. Axel Schönbeck. There, the squeezed vacuum is used in the field of Optomechanics. Further details regarding the collaboration are not provided as it is not part of this thesis.

## 4.5 Conlcusion

In the presented source for squeezed vacuum states of light, a doubly resonant hemilithic cavity design with a two temperature heating scheme was chosen for the SHG and PDC process. It was able to generate squeeze factor $>(10.5 \pm 0.1)\,\mathrm{dB}$ at a frequency of 2 MHz, which were tunable over a wavelength range of 1549.9 nm to 1550.34 nm with a maximum squeeze factor of $(11.0 \pm 0.1)\,\mathrm{dB}$. The tuning range was limited by the tuning range of the master laser. At a frequency of 50 MHz, a squeeze factor of approximately 5 dB was observed. With the coherent control locking scheme, the squeeze phase was kept stable over a time period of 8 hours. By using fibre optics for the coherent control locking scheme and omitting a mode cleaner cavity for the local oscillator, the experiment could be conducted on a more compact 60 cm x 40 cm breadboard.

The possibility to tune the wavelength of the system increases the flexibility for experiments in the range of the telecommunication wavelength of 1550 nm. Utilizing the coherent control system, the stable generation of squeezed states during a normal workday is given. In principle, this locking technique also enables to measure squeezed states of light in the audio frequency range. With the small footprint and the possibility to connect a master laser via fibre coupling, easy transportability between applications is given.

# Chapter 5

# Interferometric mirror surface characterisation

Roughness of a mirror surface leads to scattering [ERB80], which introduces noise in the audio band frequency range [VCDS07], in which current gravitational wave detectors operate. Additionally, point-like absorbers can become a limiting factor for gravitational wave detectors due to thermoelastic deformation of the test mass surface when exposed to high-power laser light [JYK$^+$21] [BVY$^+$21]. Here, a proof-of-principle Mach-Zehnder interferometric approach is presented to characterize the roughness and point-like absorbers of mirror surfaces. Commonly used commercial characterization techniques have a trade-off between up to atomic-level resolution and a narrow field of view. For example, atomic force microscopy [EW10] provides high lateral resolution but a limited field of view, while coherence scanning interferometry [PCL10] provides a wider field of view but lower resolution. By scanning a highly focused laser beam over a sample, the presented imaging technique combines up to diffraction-limited lateral resolution with the sensitivity of an interferometer. The experiment was conducted by Leif Albers [Alb23] for his master's thesis under my supervision. The results are summarized here, and a manuscript titled *Laser Scanning Microscopy for Tomographic Imaging of Roughness and Point Absorbers in Optical Surfaces* has been submitted to Advanced Devices and Instrumentation. A preprint can be found on the arXiv [AHS23]. The illustrations presented here are mostly taken from these two sources.

## 5.1 Theoretical description

Before presenting the experiment and its results, it is critical to provide a short theoretical description of a Mach-Zehnder interferometer and the interaction of a light beam with mirror coating. This will aid in understanding the measurement signals.

### 5.1.1 Mach-Zehnder interferometry

An interferometric measurement converts a phase signal on a light field into an amplitude modulation detectable by photo diodes. In the Mach-Zehnder interferometer configuration, depicted in figure 5.1, a coherent beam is split on a balanced beam spitter into a signal and reference beam. As they propagate, the signal beam acquires an additional signal phase upon reflection off the sample mirror. The two beams are overlapped spatially onto a second beam splitter, resulting in an interference signal that is dependent on the phase between the signal and reference beams.

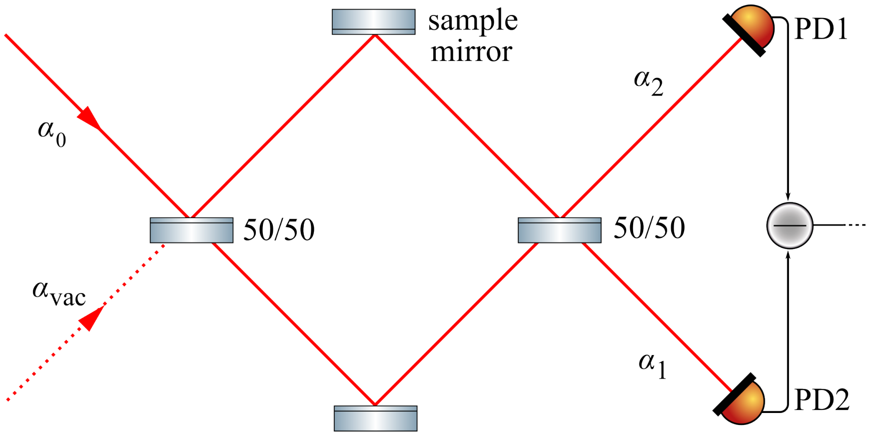

**Fig. 5.1: Priciple of a Mach-Zehnder interferometer.** A beam is split on a balanced beam splitter into a signal and reference path. The signal path includes a sample mirror that introduces a phase shift. The signal beam is then overlapped with the reference beam on a second balanced beam splitter, resulting in an interference signal that depends on the phase difference between the two arms. Two photo diodes detect the signal.

For a classical description of the Mach-Zehnder interferometer, the coherent beam can be described by a classical electromagnetic wave

$$\alpha = |\alpha|e^{i\varphi} \tag{5.1}$$

with $|\alpha|^2$ being proportional to the intensity. The balanced beam splitters can be modelled by the matrix

$$M_{BS} = \frac{1}{\sqrt{2}} \begin{pmatrix} 1 & 1 \\ 1 & -1 \end{pmatrix} \tag{5.2}$$

with a phase flip on the reflected beam. Two states enter the interferometer. Firstly, the coherent source beam $\alpha_0$ with $|\alpha_0|^2 \propto I_0$ and secondly a vacuum state $\alpha_vac$ through the empty port. While propagating through the interferometer, the light picks up phases at the beam splitters and in the interferometer arms. For the signal arm, the light picks up a signal phase $\varphi_{signal}$ and phase due to the arm length $\varphi_{L,s}$. The reference arm only picks up a phase due to the arm length $\varphi_{L,r}$. Thus, a propagation matrix can be formulated as

$$M_{prop} = \begin{pmatrix} e^{i(\varphi_{L,s}+\varphi_{signal})} & 0 \\ 0 & e^{i(\varphi_L,r)} \end{pmatrix}, \tag{5.3}$$

which leads to the following calculation for the exiting light field $\alpha_1$ and $\alpha_2$:

$$\begin{pmatrix} \alpha_1 \\ \alpha_2 \end{pmatrix} = M_{BS2} \cdot M_{prop} \cdot M_{BS1} \cdot \begin{pmatrix} \alpha_0 \\ \alpha_{vac} \end{pmatrix} = \frac{\alpha_0}{2} \begin{pmatrix} e^{i(\varphi_{L,s}+\varphi_{signal})} + e^{i\varphi_{L,r}} \\ e^{i(\varphi_{L,s}+\varphi_{signal})} - e^{i\varphi_{L,r}} \end{pmatrix}. \tag{5.4}$$

Since only a classical description was taken into account, the effects of the vacuum contribution can be neglected. The intensities at the photo diodes detecting the field calculate to

$$I_1 \propto |\alpha_1|^2 \propto \frac{I_0}{2}(1 + \cos(\varphi_{signal} + \varphi_L)) \tag{5.5}$$

$$I_2 \propto |\alpha_2|^2 \propto \frac{I_0}{2}(1 - \cos(\varphi_{signal} + \varphi_L)) \tag{5.6}$$

with $\varphi_L = \varphi_{L,s} - \varphi_{L,r}$ being the phase difference due to the path lengths. Since the photo diodes are part of a homodyne detector in the experiment, it follows for the differential signal

$$\Delta I = I_1 - I_2 \propto 2\cos(\varphi_{signal} + \varphi_L). \tag{5.7}$$

Here it can be seen, that the Mach-Zehnder interferometer's signal is indeed phase dependent allowing the detection of $\varphi_{Signal}$. The phase sensitivity of a coherent light

Mach-Zehnder interferometer is given by the equation [DDJK15, p.21]

$$\Delta\varphi = \frac{1}{\sqrt{\langle\bar{n}\rangle}|sin(\varphi_{signal} + \varphi_L)|}. \tag{5.8}$$

Thus, the sensitivity increases with the intensity of the coherent light field and the interferometer operates optimal at the points $\varphi = \pi/2$, $\varphi = 3\pi/2$. The operating point $\varphi = \pi/2$ is called *mid-fringe*.

### 5.1.2 The measured phase profile

High reflectivity mirror coatings usually consists of alternating layers of two materials with low and high refractive indices $n_l, n_h$. When coherent light is incident on such a high reflection coating, part of the light transmits through the first interface and is reflected at deeper layers.

In order to achieve a maximum reflectivity, it is desired for the light reflected at deeper layers to interfere constructively with previous reflected light. This is achieved by choosing a layer thickness of a quarter wavelength. Therefore, reflections of multiple layers inside the coating contribute to a signal in a measurement. According to Beer-Lamberts law, the intensity of the beam decreases exponentially with coating depth [Swi62]. This implies that deeper layers contribute less to the signal. In fact, a phase penetration depth $L_\tau$ can be calculated for a distance inside the coating, in which the light acquires a significant contribution to the reflection phase [BC92]. In the presented experiment, the phase penetration depth can be approximated to $L_\tau \approx 0.9\,\mu\text{m}$. In this experiment, the coherent laser beam has a Gaussian shape, which has to be considered for the interaction. Thus, all phase contributions within the interaction volume are reduced to an effective phase value. By moving the beam over the investigated area, an effective phase profile can be measured. Figure 5.2 depicts a two-dimensional interaction between a coherent beam and a coating to understand the effective phase profile. Here, the coating is illuminated through the mirror substrate, as it is the case in the later-presented experiment.

While the beam scans the surface along the x-axis, it picks up a phase due to the surface roughness $\varphi_R(x)$ and volumetric effects $\varphi_V(x,z)$. Both phases are projected onto the x-axis as a phase profile $\varphi_z(x)$. Since the probe beam is Gaussian, the intensity profile is non uniform. The phase profile is a convolution of the projected phase profile and Gaussian beam profile

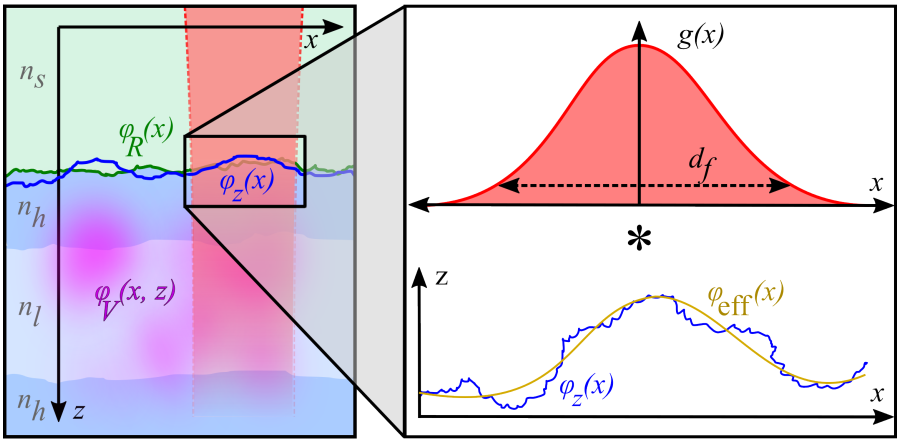

**Fig. 5.2: The effective phase profile.** The left side shows a cross section of a beam interacting with a coating. Inside the coating, the beam accumulates a phase due to the surface profile $\varphi_R(x)$ and volumetric effects $\varphi_V(x, z)$, resulting in a surface profile $\varphi_z(x)$. On the right, the effective phase profile $\varphi_{eff}(x)$ is obtained through a convolution of the phase profile with the Gaussian beam intensity $g(x)$.

$$g(x) = A_x e^{-\frac{2x^2}{\sigma_x^2}}, \tag{5.9}$$

resulting in a smoothed effective phase profile

$$\varphi_{eff}(x) = \varphi_z(x) * g(x). \tag{5.10}$$

The lateral resolution is limited by the fact that features smaller than the beam diameter cannot be properly resolved.

For a more simplified description, the effective phase profile can be converted into a displacement profile, where the beam must travel a certain distance $\Delta z$ to accumulate the same phase. Considering the reflection under normal incidence, the effective phase can be expressed as

$$\varphi_{eff} = 2kn_s\Delta z \tag{5.11}$$

with the wave number $k$ and the refractive index of the substrate $n_s$. The introduced displacement can be understood as an elevation or reduction from a perfectly flat effective phase profile at the boundary layer between substrate and coating. Therefore, the average deviation can be considered as an *effective roughness* acting on the beam.

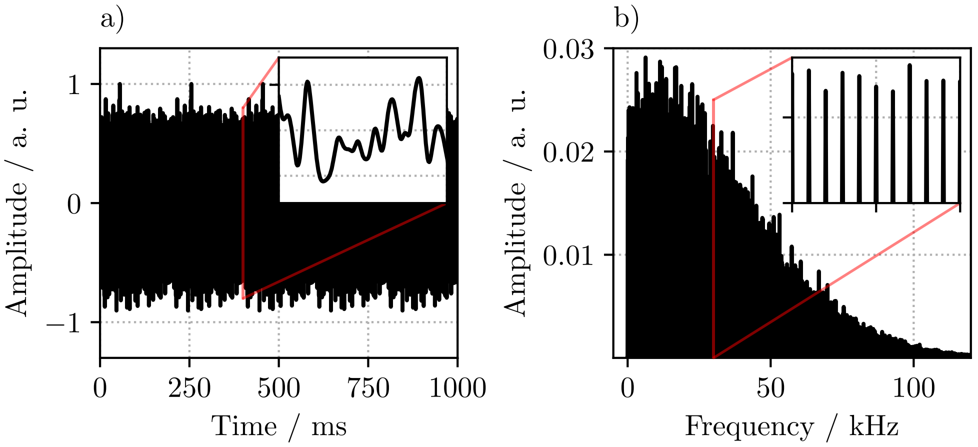

**Fig. 5.3: Expected Signal.** The left shows a temporal signal with a period of $T = 1/f_{rot}$. Zooming into the peaks shows the smoothing due to the convolution with a Gaussian. On the right, the corresponding spectrum consisting of a frequency comb enveloped by a Gaussian is depicted.

Unlike surface roughness, which is a solid surface profile, the effective roughness takes into account all possible phase changes for a beam interacting with the coating.

### 5.1.3 The expected signal

To get a theoretical concept of the expected signal, a circular scan over a a surface at fixed radius is considered. Thus, the signal looses the spatial dependency and only depends on the acquisition time $t$. In an ideal case, a rough surface does not have spatial structure with its signal only consisting of random phase changes similar to white noise. The signal repeats itself with a rotation frequency $f_{rot}$ and can therefore be described as a periodic function $s(t)$ with a period $T = 2\pi/f_{rot}$. With a Fourier transform, this temporal signal $s(t)$ can be converted into a frequency spectrum [Coh95]. The Fourier transform is defined as

$$(\mathcal{F}s)(f) = \int_{-\infty}^{\infty} s(t) e^{2\pi f t} dt. \tag{5.12}$$

Since $s(t)$ is a periodic function, it can be expressed by its Fourier series

$$s(t) = \sum_{n=-\infty}^{\infty} = c_n e^{2\pi i n t/T}, \quad c_n = \frac{1}{T} \int_0^T s(t) e^{-\frac{2\pi i n t}{T}} dt \tag{5.13}$$

leading to the Fourier transformation

$$(\mathcal{F}s)(f) = \sum_{-\infty}^{\infty} c_n \int_{-\infty}^{\infty} e^{-2\pi i (f-\frac{n}{T})t} dt \tag{5.14}$$

$$= \sum_{-\infty}^{\infty} c_n \delta(f - n/T). \tag{5.15}$$

This expression reveals, that the frequency spectrum is given by a frequency comb with peaks of the amplitude $c_n$ and spaced apart by $f_{rot} = 1/T$. As before, the Gaussian intensity profile in the measurement process has to be considered. Thus, the signal $s(t)$ has to be convolved with a temporal Gaussian profile. The convolution theorem for Fourier transform states

$$(\mathcal{F}(s * g))(f) = (\mathcal{F}s)(f) \cdot (\mathcal{F}g)(f). \tag{5.16}$$

Hence, to calculate the convolution, the Fourier transform of the signal needs to be multiplied with the Fourier transform of the Gaussian profile. The Fourier transform of a Gaussian is still a Gaussian and can be given here as

$$(\mathcal{F}g)(f) = A_t \int_{-\infty}^{\infty} e^{-\frac{2t^2}{\sigma_t^2}} e^{-2\pi i f t} dt \tag{5.17}$$

$$= A_f e^{\frac{-2f^2}{\sigma_f^2}}. \tag{5.18}$$

with the amplitude $A_f = \sigma_t A_t \sqrt{\pi/2}$ and spectral width $\sigma_f = 2/\pi\sigma_t$. For the Fourier transform of the measured signal follows

$$(\mathcal{F}s * g)(f) = A_f e^{-\frac{2f^2}{\sigma_f^2}} \cdot \sum_{n=-\infty}^{\infty} c_n \delta(f - \frac{n}{T}). \tag{5.19}$$

Here, the spectrum consisting of a frequency comb is enveloped by a Gaussian profile. Therefore, the spectral range for measurable signals is determined by the Gaussian envelope and can be calculated with the relation

$$\sigma_t \sigma_f = \frac{\pi}{2}. \tag{5.20}$$

The temporal beam width depends on how fast the laser beam traverses a fixed point on the mirror surface and is given by

$$\sigma_t = \frac{d_f}{2v_{beam}} = \frac{d_f}{4\pi r f_{rot}}, \tag{5.21}$$

where $d_f$ is the beam diameter, $v_{beam}$ denotes the beam's velocity with respect to the surface, and $r$ is the radius of the trajectory. Thus, the spectral range increases with a smaller focus, larger rotation frequency and trajectories further away from the mirror center. In figure 5.3, a simulated temporal signal and a spectrum for a random repeating signal at a rotation frequency of $f_{rot} = 5\,\text{Hz}$, a radius of 10 mm and a focus of 2 µm is shown. The corresponding spectral width is $\sigma_f = 100\,\text{kHz}$. This gives an estimation for the expected frequency range in the experiment, in which signals occur.

## 5.2 Setup

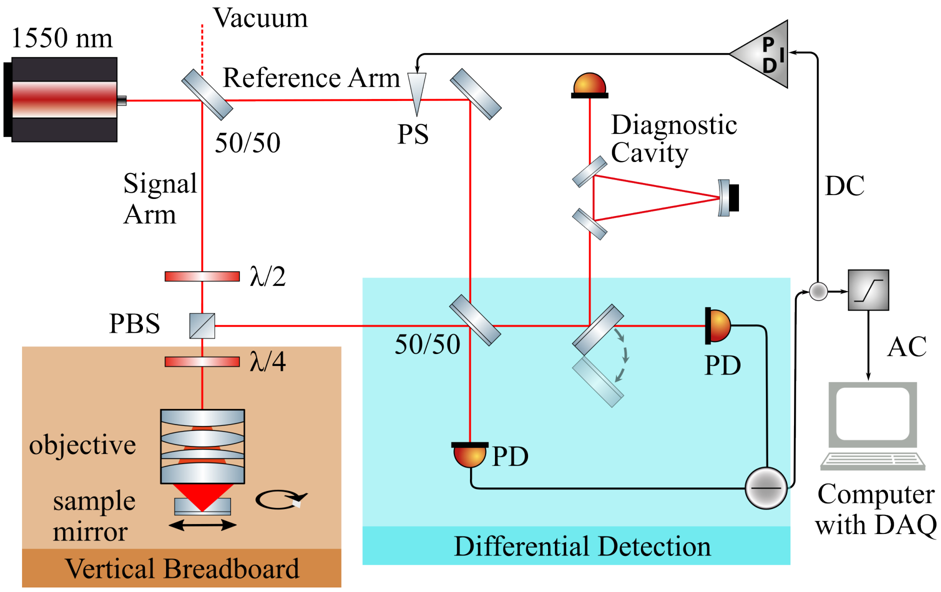

**Fig. 5.4: Scheme of the surface characterisation setup.** The 1550 nm light was split equally at a beam splitter in a signal and reference beam path. In the signal path the beam was focused on the rotating mirror (orange box). With combination of a quarter wave plate and a polarizing beam splitter the signal carrying light was directed to differential detection (blue section). Here, the signal beam was overlapped on a second 50/50 beam splitter with the reference beam. The signal's DC part was fed back to phase shifter in the reference beam path to lock the interferometer. The AC part was recorded with a data acquisition card.

A schematic of the experimental setup of the Mach-Zehnder interferometer is depicted in figure 5.4. An NKT Basik laser module provided 1550 nm light, which was divided equally at a 50/50 beam splitter into a reference arm and a signal arm. In the signal arm, a 0° high reflective mirror with a diameter of 25.4 mm coated by 3Photon, was used as a sample. It was 6.35 mm thick and the backside featured an anti-reflective coating. The manufacturer specified the reflectivity to 99.95 % and the surface roughness to <800 pm. The mirror was mounted on a rotation stage, which itself could be moved by a linear stage. This enabled scans to be performed at fixed radii from the center or in spirals across the surface. The beam was focused with an objective to a waist of $(5.29 \pm 0.06)\,\mu\mathrm{m}$. Since the objective was designed to focus a beam through a 6.35 mm substrate for an application in a different experiment, the beam entered the mirror through the substrate and was focused on the interface between the substrate and coating. The objective and a periscope were mounted on a vertical breadboard to focus the beam onto the mirror, which was elevated above the beam height due to the motion stages. A combination of a polarizing beam splitter and a quarter wave plate isolated the signal-carrying retro reflected light and directed it to a differential detection, where it was overlapped with the reference beam on a second 50/50 beam splitter. Here, a homodyne detector was used as a differential photo diode for the detection. The DC signal was fed back to a phase shifter to lock the interferometer on mid-fringe, while the AC signal was fed to a data acquisition card (DAQ) for signal recording. The DAQ had a resolution of 16 bit and a sampling rate of 3.571 MSa/s.

### 5.2.1 Low frequency homodyne detector

A homodyne detector was used as a differential PD in this setup. It is crucial to note, that not balanced homodyne detection was performed in this setup. Due to the equal light power in the signal and reference beam, the homodyne approximation was not valid any more. However, the detector had to operate in a frequency range of up to 100 kHz, in which signals were expected. To estimate the linearity, the noise power spectra of the reference arm's light were measured with a network analyser in the frequency range of 0 Hz to 100 kHz and are depicted in figure 5.5. Doubling the light power led to a 3 dB increase in the noise level, indicating a linearity up to 2 mW.

The detector exhibited a dark noise clearance of 19 dB, as depicted in figure 5.6(a). Small peaks were visible in the dark noise, which were caused by pick up of communication signals at 19.6 kHz and 20 kHz and their harmonics via the cables acting as antennas. However, measurements to characterize the surface were taken using a data acquisition card. Here, the dark noise clearance was limited to 5.8 dB by the

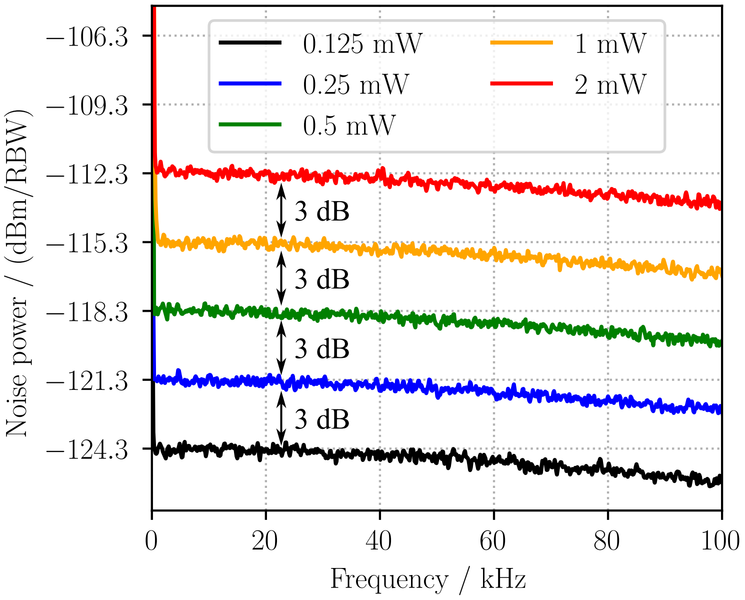

**Fig. 5.5: Linearity of the low frequency homodyne detector.** Spectra were measured in frequency range of 0 Hz to 100 kHz at light powers up to 2 mW. The noise level increased by 3 dB for doubling the light power indicating a linear homodyne detector. The resolution bandwidth of the network analyzer is 128 Hz

electronic noise floor of the card itself. In addition to the pick up of communication signals, there are peaks in the dark noise most likely due to electronic reflection inside the cables as result of imperfect impedance matching. These peaks also appear in the shot noise. To keep the contribution to the shot noise minimized, the light power had to be at least 0.5 mW.

### 5.2.2 Control loop

As previously stated, the Mach-Zehnder interferometer achieves the highest phase sensitivity when operated at mid-fringe. Disturbances can cause the interferometer to deviate from the optimal operating point. Those disturbances arose, for instance, from the motion stages' movement and air fluctuations. The resulting additional phase shifts led to an increased signal measured by the detector. To counteract the disturbances, the signal was fed back to a phase shifter via a PID controller for frequency shaping. An open-loop gain measurement depicted in 5.7 shows the maximum control loop bandwidth of 5 kHz. The control loop was able to suppress disturbances arising from the spinning of the rotation stage at frequencies up to 5 Hz. However, the maximum light power in the interferometer was limited by the control loop, as the signal resulting from disturbances also increased with the light power. Here, disturbances could not compensate for at light powers exceeding 0.55 mW.

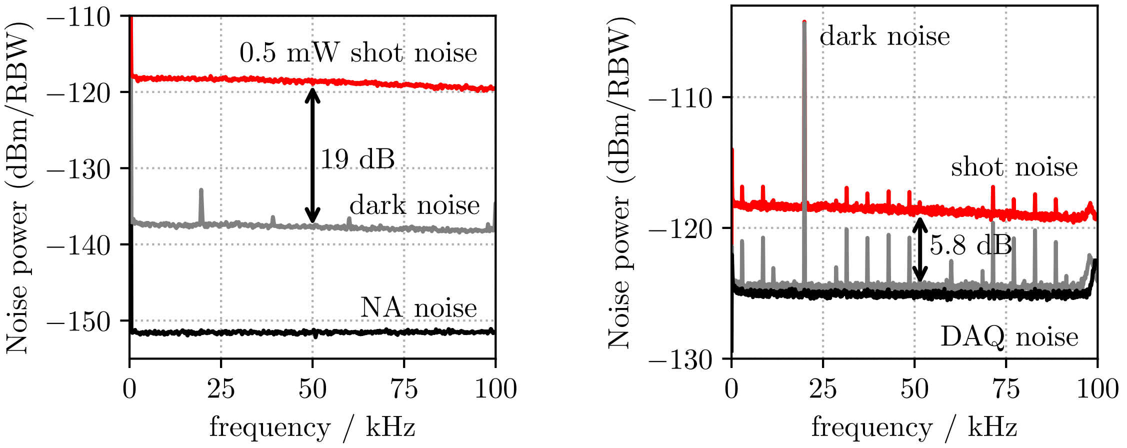

(a) Dark noise clearance measured with a Network analyzer.

(b) Dark noise clearance measured with the data acquisition card.

**Fig. 5.6: Dark noise clearance of the low frequency homodyne detector.** On the left, a measurement with a network analyser yields a dark noise clearance of 19 dB at a light power of 0.5 mW in the reference arm. On the right, the dark noise clearance for the data acquisition card is limited by the cards digitalization noise to 5.8 dB. All traces were averaged 1000 times. The resolution bandwidth was 128 Hz for the network analyser and 56 Hz for the data acquisition card.

Thus, all measurements in this chapter were taken at a light power of 0.5 mW.

### 5.2.3 Interferometer sensitivity

The interferometer sensitivity is typically expressed by the amplitude spectral density (ASD) in the units of $\mathrm{m}\sqrt{\mathrm{Hz}}$. However, since the homodyne detector measured signal in voltage, a calibration between voltage and phase was required. Equation 5.8 states that the signal is given by a sinusoidal function. Only small changes around 0 needed to be considered, since the phase change of the specified roughness of 800 pm was significantly smaller than $\pi/2$, which corresponds to a phase signal of a 390 nm elevation. Therefore, the sinusoid was approximated around 0 by a linear slope, and its gradient was used as a calibration constant. Figure 5.8 shows the amplitude spectral density for shot noise, technical noise, and signal measurement. To measure the technical noise, the interferometer signal was measured with a stationary sample mirror. It is clearly visible, that the interferometer was not shot noise limited and the technical noise increased for frequencies below 20 kHz. It was not surprising for the interferometer not being shot noise limited in the audio band regime, since several noise sources could couple into this frequency region. Noise sources coupling into a balanced homodyne detection in the audio band region presented in [SMLC$^{+}$12] also

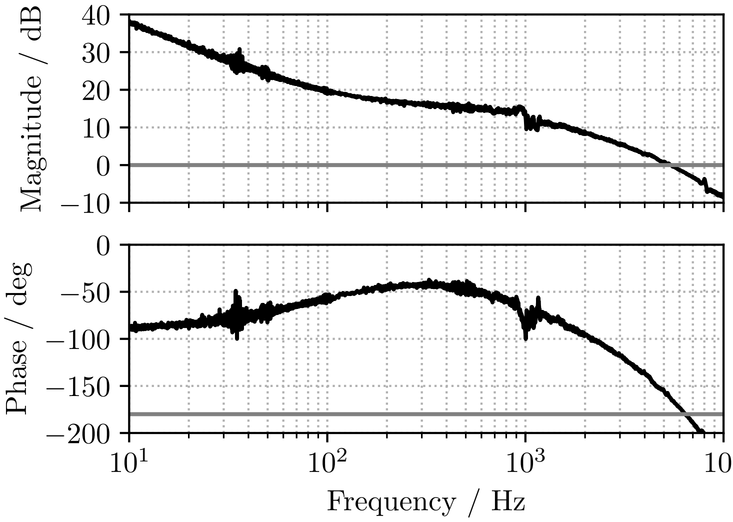

**Fig. 5.7: Open loop measurement of the interferometer control loop.** The bode plot of the control loop shows a response with a unity gain of 5 kHz. Disturbances with higher frequencies could not be compensated for.

apply for the Mach-Zehnder interferometer, especially the air fluctuations and audio noise, since the experiment was not properly decoupled from the surrounding with a steel tank. To reduce the contribution of stray light, super polished optics should be used. It is possible that electronic noise, such as that from the motion stages and power supply rack, is contributing to the noise floor. However, the signal to noise ratio remained at 32 dB on average for frequencies below 60 kHz. A maximum interferometer sensitivity, where also a signal was observed, of $(3.1 \pm 1.2)\,\mathrm{fm}/\sqrt{\mathrm{Hz}}$ was reached at a frequency of 40.9 kHz, which is close to the shot noise limited resolution of $(2.5 \pm 1.2)\,\mathrm{fm}/\sqrt{\mathrm{Hz}}$.

For the signal trace measurement, the mirror was rotated at a frequency of $f_{rot} = 5\,\mathrm{Hz}$ at a radial distance of $r = 4.5\,\mathrm{mm}$. Below 2.5 kHz, the signal data was dominated by noise and had to be filtered out by a spectral filter. The spectral filter set all contributions between 0 Hz and 2.5 kHz to 0. By filtering the low frequencies, information on large scale structures got lost and gave an upper size limit for observable structures. This limit can be calculated by converting the time period $T$ in spatial period $T_{spatial}$:

$$T_{spatial} = \frac{1}{f_{spatial}} = \frac{u f_{temporal}}{T} = \frac{2\pi r f_{temporal}}{T}. \tag{5.22}$$

For the spectral filter of 2.5 kHz, lateral structure spanning over 56.22 µm could not be resolved.

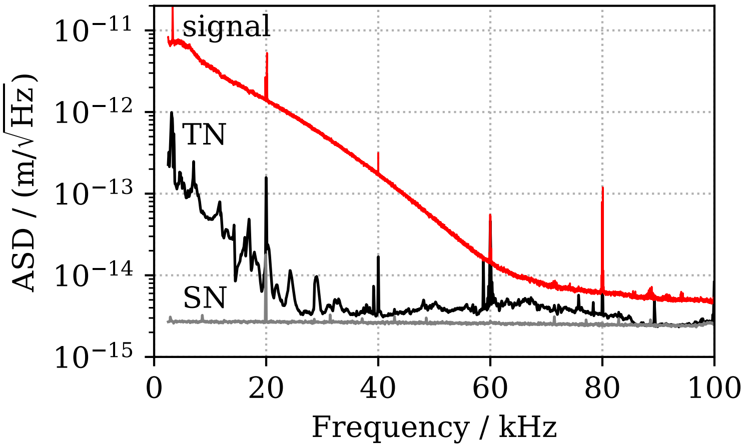

**Fig. 5.8: Interferometer sensitivity.** The amplitude spectral density is depicted for the shot noise (SN), technical noise (TN) and signal measurement. The technical noise was measured with a stationary sample mirror. Below 60 kHz, the average signal to noise ratio was 32 dB. A Sensitivity of up to $(3.1 \pm 1.2)\,\mathrm{fm}/\sqrt{\mathrm{Hz}}$ was achieved. All traces were averaged over 1000 traces and were measured with a resolution bandwidth of 53 Hz for TN and SN, 5 Hz for the signal.

## 5.3 Phase measurement

Scanning the coating in a spiral pattern allowed to derive a two-dimensional map of the scanned area. For this purpose, the mirror was rotated at $f_{rot} = 5\,\mathrm{Hz}$ while simultaneously moving linearly at a constant velocity of $v_r = 10\,\mu\mathrm{m/s}$. Each sample $j$ was assigned a polar coordinates by

$$r_j = r_0 + v_{beam} j \Delta t \tag{5.23}$$

$$\varphi_j = \varphi_0 + 2\pi j \Delta t, \tag{5.24}$$

which was afterwards transformed into Cartesian coordinates. The pixel size for the image was set to $2\,\mu\mathrm{m}$, which is the distance the beam travelled along the radial axis after one revolution. A smaller pixel size could lead to empty pixels, as it would no longer be guaranteed for a pixel to contain samples. The value assigned to each pixel was the mean over all samples falling into its boundaries.

Figure 5.9 shows a reconstructed effective roughness map for an annular section between the radii $r_0 = 3.5\,\mathrm{mm}$ and $r_{end} = 5.5\,\mathrm{mm}$ of the surface, where the surface level is given by displacements from the mean value. Artefacts due to noise filtering are visible at the bottom of the annular map. The roughness profile of the surface is revealed by enlarging a section in (a) by a factor of 10 in (b). Enlarging the image

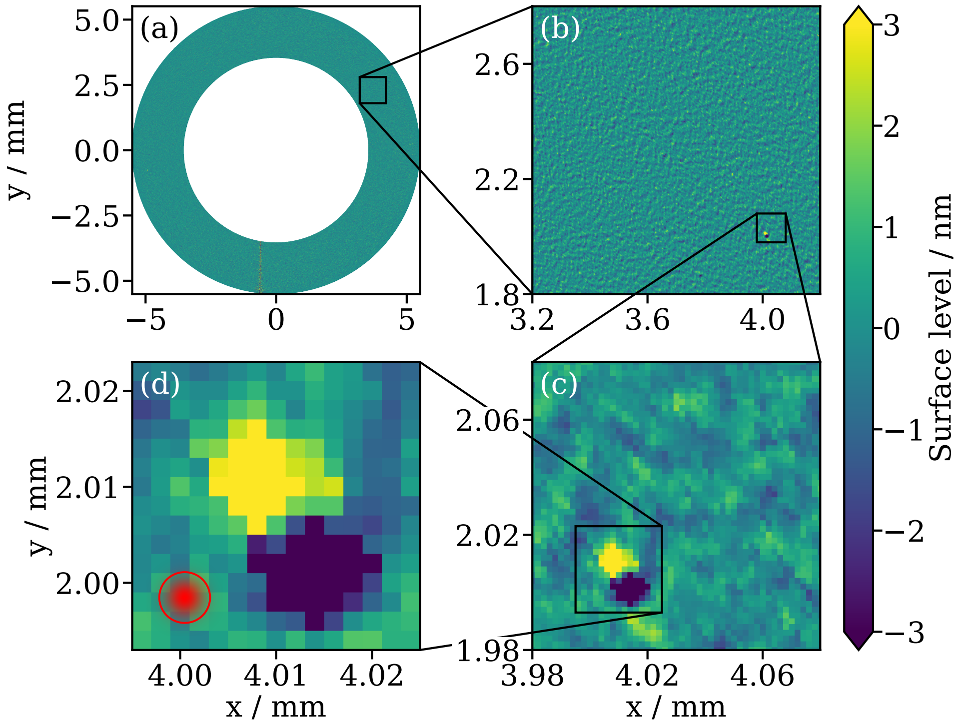

**Fig. 5.9: Map of the surface roughness.** The two-dimensional map shows the effective roughness for a 56 mm$^2$ area in terms of deviations from a mean surface level for a lateral resolution of 5.29 µm. (a) provides an overview of the circular scan area with a thickness of 2 mm. An enlargement by the factor of 10 in (b) shows the effective roughness of the surface. Macroscopic features become visible in (c) after further enlargement by a factor of 10. In (d), the macroscopic feature is compared with the beam size after another enlargement by a factor of 3. The area was scanned in 200 seconds

again by a factor of 10 in (c) revealed macroscopic features in the profile. In (d), a comparison is made between the size of a macroscopic feature and the beam size after an enlargement by a factor of 3. All macroscopic features over the scanned area showed oscillations between positive and negative surface levels along the radial axis. These oscillations may be attributed to the spectral filter, as they were found to be correlated with the threshold frequency. The measurement was limited to an annular excerpt of the area due to a tilt of the linear stage. Moving the stage caused the beam to be defocused on the examined coating-substrate interface. Consequently, the size of the reflected beam changed, leading to a reduced mode overlap with the reference beam. Ultimately, the decreased mode overlap caused a the control loop to fail as it depended on the interference signal.

The surface roughness is typically specified by the root mean square error (RMS) relative to the mean elevation $\bar{z}$ and can be calculated by

$$\mathrm{RMS} = \sqrt{\frac{1}{N}\sum_{j=1}^{N}(z_j - \bar{z})^2}, \tag{5.25}$$

where $N$ denotes the total number of samples and $z_j$ the deviation of a sample $j$ [Ben07]. For the measurement shown in figure 5.9, the RMS was value calculated to 590 pm. In order to estimate the deviation, the RMS over all samples inside a pixel was calculated for each pixel in the map. The deviation for the complete map was then estimated by taking the mean of the previously calculated RMS values of all pixels:

$$\epsilon = \frac{1}{N_{Pixel}}\sum_{j=1}^{N_{Pixel}} s_j. \tag{5.26}$$

Using this approach the effective roughness was quantified as (590 ± 29) pm. This result is in good agreement with the manufacturers specified surface roughness of <800 pm. It was not expected to have such a strong agreement since this method measures the effective roughness and not the atomic surface.

The circular excerpt was measured in 200 seconds. Thus, a scanning time of 20 minutes can be approximated for the characterisation of the complete surface.

## 5.4 Optical loss measurement

Using only one photo diode in the presented setup, the DC signal yielded the possibility to gain insight into the optical loss of the inspected coating. A relative measurement is presented, since the photo diode was not calibrated to the light power. The loss was determined by normalizing the value of a pixel to the mean over the complete scanned area, with the rms deviation subtracted beforehand to correct the values for detection noise. Similar to the phase measurement, a spectral filter at a cut off frequency of 0.5 kHz was used to remove the background. Figure 5.10 displays a reconstructed two-dimensional map of the loss over the same area as in the roughness map in figure 5.9 from the previous section. The same area was enlarged in (b), (c) and (d) with the same factors revealing that the macroscopic feature was also an absorber. In (d), the size of the feature is compared with the beam size. The macroscopic features in the loss map caused an optical loss of up to 65 % over the beam area of 22 $\mu\mathrm{m}^2$. These features appeared in a density of 12 spots per $\mathrm{mm}^2$. Calculating the mean optical loss over the complete scanned area resulted in a reflec-

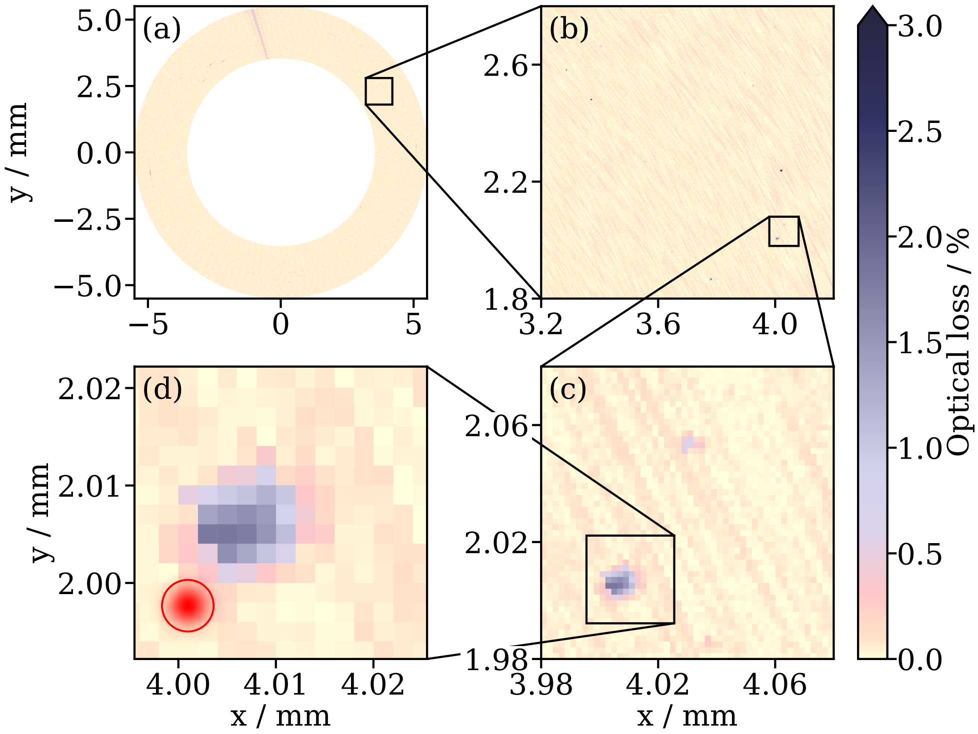

**Fig. 5.10: Map of the surface's optical loss.** The two-dimensional map shows the optical loss for the same area and same lateral resolution as in 5.9. The pictures in (b), (c), and (d) are enlargements of the same area and factors as before. The macroscopic feature in (c) clearly indicates a point of optical loss and is compared to the beam size in (d).

tivity of (99.88±0.02) %. The spots of high loss might be a result of included particles between the substrate and coating during the coating process. Excluding them in the calculation to give an estimation of the reflectivity on the mirror's surface resulted in a value of (99.95 ± 0.02) %, which fits well with the manufacturer's specification of 99.95 %.

## 5.5 Correlation between loss and effective roughness measurement

Upon closer inspection of the macroscopic features in the loss and roughness map, it was revealed that most of them appeared in both maps at the same position. However, some features only appeared in one of the maps. These occurrences are illustrated in figure 5.11, which depicts the same excerpt of both maps. This emphasizes that the features had different origins depending on the map they appeared in.

Features that only appeared in the roughness map were solely a result of a phase changes in the light. Defects primarily causing this type of defect could be steps in

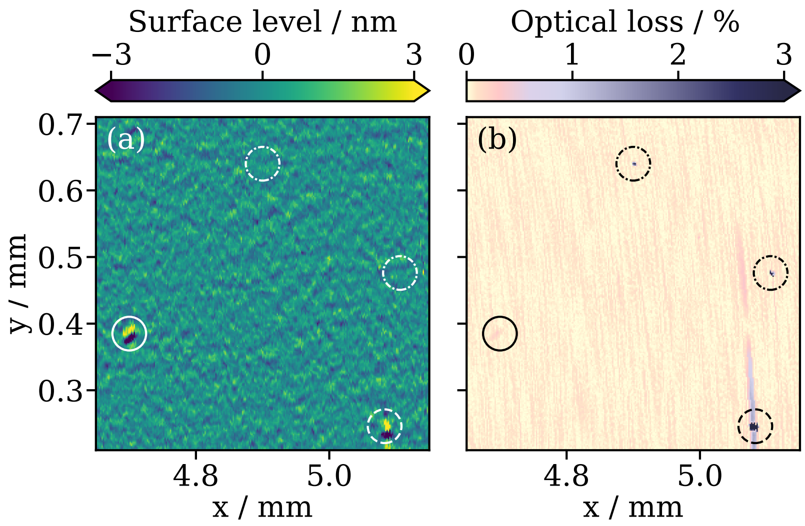

**Fig. 5.11: Correlation between optical loss and effective roughness measurement.** The roughness and loss map display the same excerpt of the scanned area, including some macroscopic features. The feature circled in solid lines only appeared in the roughness map, indicating a defect that only affected the light's phase, such as a step in the atomic layer. The feature circled in dash-dotted lines only appeared in the loss map, suggesting a point-like absorber. Features in circled with dashed lines appeared in both maps originating, for instance, from point scatterers.

the atomic profile or changes in the refractive index.

If a feature appears in both maps, the light had to be significantly effected by a phase change and loss. Scattering defects could cause both of these effects.

Peaks that experience loss without a phase change only appeared in the loss map. They could be caused by point-like absorbers and hold a special interest in high-power applications, as they heat up the mirror. This introduces the possibility of a locally distorted surface causing increased scattering upon reflection.

## 5.6 Conclusion

The Mach-Zehnder interferometer presented in this study was used to analyze a mirror surface with a lateral resolution of $(5.29 \pm 0.06)\,\mu\mathrm{m}$ and a sensitivity of $(3.1 \pm 1.2)\,\mathrm{fm}/\sqrt{\mathrm{Hz}}$. Circular scans at a fixed radius and spiral scans over a sample mirror were enabled by a linear and a rotational motion stage. Two-dimensional maps of the surface roughness and optical loss of the coating were generated using a digital reconstruction algorithm. The effective roughness and reflectivity were determined using these maps to be $(590 \pm 29)$ pm and $(99.95 \pm 0.02)\,\%$, respectively, which confirms the manufacturer's specifications. Additionally, point absorbers were identified in the coating, which may cause surface distortions in high laser power applications.

The coating was analyzed through the substrate due to the design of the focusing objective, but this setup is not limited to this configuration. It is important to note that the phase measurement did not determine the actual surface roughness, but rather the interaction between the light and the coating. In this proof of principle experiment, only a circular excerpt with an area of $56\,\mathrm{mm}^2$, limited by the alignment of the linear stage, was scanned in 200 seconds. However, it can be estimated that a full 1 inch mirror would take approximately 20 minutes to scan. The sensitivity can be improved further by using squeezed states of light, once the noise floor for frequencies below 60 kHz is reduced to the shot noise limit.

# Chapter 6

# Summary and outlook

Squeezed states of light have evolved into a pillar of quantum technology. They have found applications, for instance, in quantum sensing and quantum metrology, with the most famous example being the sensitivity increase of gravitational wave detectors. However, to widen the field of possible applications, it is crucial to develop and study compact and tunable sources for squeezed states of light. Within this thesis, two different cavity designs were investigated for the applicability in compact squeezed states of light sources based on cavity enhanced parametric down-conversion at a wavelength of 1550 nm.

The first setup examined double resonant monolithic cavities, which solely consisted of a ppKTP crystal with curved and coated end faces, on an 80 cm x 80 cm breadboard. This setup generated squeezed states of light with a noise suppression of $(10.4 \pm 0.1)$ dB referenced to the vacuum noise. However, the monolithic cavities were only double resonant at specific wavelength tunings in the tens of picometre regime away from 1550 nm. These double resonant points cannot be predicted beforehand, as they depend on factors such as coating reflectivities, cavity length, crystal cut, which have inherent error margins in the manufacturing process. This rules doubly resonant monolithic cavities out, if a certain wavelength is required for an application. Especially, if two sources have to operate at the same wavelength, since two monolithic cavities do not necessarily share the same double resonant points.
For a stable generation of squeezed vacuum states, this experiments needs control loops to keep the cavities on resonance, and to keep the squeeze phase stable. After this experiment was conducted, a control loop acting on the cavity temperatures was developed for the SHG to maintain a stable conversion [Huh21]. This approach wasn't transferable to the PDC cavity. However, this problem may be circumvented by locking the master laser onto the PDC cavity. Once the cavities operate stable

on resonance, the squeeze phase can be stabilized by implementing, for instance, the coherent control locking scheme.

The second squeezed state of light source was based on double resonant hemilithic cavity design consisting of a one sided HR coated ppKTP crystal and an incoupling mirror. This cavity design allowed the generation of squeeze factors $>(10.5 \pm 0.1)\,\mathrm{dB}$ tunable over a wavelength range of roughly 0.5 nm around the 1550 nm center wavelength. Here, the tuning bandwidth was only limited by the master laser's wavelength range and cavities' fine tuning temperature range. A control loop ensured a stable average squeeze factor of $(10.2 \pm 0.1)\,\mathrm{dB}$ over a time period of 8 hours. Due to the replacement of free space optics with fibre optics and omitting obsolete parts, the experiment could be conducted on a more compact 60 cm x 40 cm breadboard.
With the wavelength tunability of the system, the wavelength of the squeezed vacuum states can simply be adjusted to the needs in a subsequent application. The stable generation over 8 hours is ensured by the coherent control locking scheme, which in general also allows to measure squeezed states in the audio frequency region. Since the master laser can easily be switch via a fibre coupler and due to the small footprint, the system can easily transported between application sites. Apart from this thesis, the presented source is lent to the ETH in Zurich with an already developed automatic control loop scheme.
However, by replacing more free space optics with fibre optics, sources for squeezed states of light can be further compactified. One option might be an fibre coupled SHG system to further reduce free space optics. Since the size of presented system is in the order of table top laser systems, the next step could be a setup fitting in a 19 inch Rack plug-in unit in commonly used Racks. Once the system fits into a Rack, the squeezed states of light must be accessible through fibre coupling. Here it is crucial, to achieve a coupling efficiency of the squeezed vacuum states into the fibre in order to minimize optical losses.

High-power laser interferometers, such as gravitational wave detectors, suffer from point absorbers enclosed in the mirror coatings, which heat up and distort the surface. In addition to the study on the generation of squeezed states of light, a Mach-Zehnder interferometer to characterize mirror surfaces was engineered within this thesis. With a lateral resolution of $(5.29 \pm 0.06)\,\mu\mathrm{m}$ and a sensitivity of $(3.1 \pm 1.2)\,\mathrm{fm}/\sqrt{\mathrm{Hz}}$, a surface could be scanned in a spiral pattern using a rotation and linear motion stage beneath the sample. This approach enabled the reconstruction of a two dimensional map of the surface roughness and the optical loss, and identified point absorbers. For a HR sample mirror, the roughness was determined to an rms value of $(590 \pm 29)\,\mathrm{pm}$ and reflectivity of $(99.95 \pm 0.02)\,\%$, which substantiated the manufacturer's specifications. Since the presented method is based on a phase measurement, the measured profile is an effective roughness correlated to the actual interaction between light and coating.

However, there is still room for improvement. The lateral resolution can be increased by focusing the laser beam down to the diffraction limit. The technical noise can be minimized by isolating the experiment from the surrounding in a steel tank. This setup can also benefit from a vacuum inside the steel tank. Furthermore the coupling of electronic noise in the measurement has to be investigated and taken care off. Once the sensitivity reaches the shot noise limit, squeezed states of light can be utilized to further increase the sensitivity. Improvements in the field of view can be achieved through better alignment of the linear motion stages. In addition to the potential for a large field of view, the presented method can scan an entire one-inch mirror in about 20 minutes. The scanning time strongly correlates with the sample's rotation frequency and lateral resolution. Overall, the presented experiment yields the possibility to be an alternative to state of the art measurement methods for high-resolution characterisation of mirror coatings.

With a second homodyne detection, a simultaneous readout of the phase and amplitude information becomes possible. In this configuration, an entangled state formed out of two orthogonal squeezed states enables an increased sensitivity for a simultaneous measurement.

# List of Figures

# Bibliography

[A$^+$11] J Abadie et al. A gravitational wave observatory operating beyond the quantum shot-noise limit. *Nature Physics*, 7(12):962–965, 2011.

[AAA$^+$19] Fausto Acernese, M Agathos, L Aiello, A Allocca, A Amato, S Ansoldi, S Antier, M Arène, N Arnaud, S Ascenzi, et al. Increasing the astrophysical reach of the advanced virgo detector via the application of squeezed vacuum states of light. *Physical review letters*, 123(23):231108, 2019.

[AGML16] Ulrik L Andersen, Tobias Gehring, Christoph Marquardt, and Gerd Leuchs. 30 years of squeezed light generation. *Physica Scripta*, 91(5):053001, 2016.

[AHS23] Leif Alber, Malte Hagemann, and Roman Schnabel. Laser scanning microscopy for tomographic imaging of roughness and point absorbers in optical surfaces. *arXiv preprint arXiv:2310.14847v2 [physics.optics]*, 2023.

[Alb23] Leif Albers. Interferometric setup for profiling and characterization of mirror surfaces. Master's thesis, Universität Hamburg, 2023.

[AMS13] Stefan Ast, Moritz Mehmet, and Roman Schnabel. High-bandwidth squeezed light at 1550 nm from a compact monolithic ppktp cavity. *Optics Express*, 21(11):13572–13579, 2013.

[ANS$^+$11] Stefan Ast, Ramon Moghadas Nia, Axel Schönbeck, Nico Lastzka, Jessica Steinlechner, Tobias Eberle, Moritz Mehmet, Sebastian Steinlechner, and Roman Schnabel. High-efficiency frequency doubling of continuous-wave laser light. *Optics letters*, 36(17):3467–3469, 2011.

[B$^+$14] Massimo Bassan et al. Advanced interferometers and the search for gravitational waves. *Astrophysics and Space Science Library*, 404:275–290, 2014.

[Bau16] Christoph Baune. *Frequency up-conversion of nonclassical states of light.* PhD thesis, Gottfried Wilhelm Leibniz Universität Hannover, 2016.

[BC92] Dubravko I Babic and Scott W Corzine. Analytic expressions for the reflection delay, penetration depth, and absorptance of quarter-wave dielectric mirrors. *IEEE Journal of Quantum Electronics*, 28(2):514–524, 1992.

[Ben07] Jean M Bennett. Characterization of surface roughness. In *Light scattering and nanoscale surface roughness*, pages 1–33. Springer, 2007.

[BGS$^+$15] Christoph Baune, Jan Gniesmer, Axel Schönbeck, Christina E Vollmer, Jaromír Fiurášek, and Roman Schnabel. Strongly squeezed states at 532 nm based on frequency up-conversion. *Optics Express*, 23(12):16035–16041, 2015.

[Bla01] Eric D Black. An introduction to pound–drever–hall laser frequency stabilization. *American journal of physics*, 69(1):79–87, 2001.

[Boy08] Robert W Boyd. *Nonlinear Optics.* Elsevier Inc, 3rd Edition 2008.

[BRF97] A S Bell, E Riis, and A I Ferguson. Bright tunable ultraviolet squeezed light. *Optics Letters*, 22(8):531–533, apr 1997.

[BVY$^+$21] Aidan F Brooks, Gabriele Vajente, Hiro Yamamoto, et al. Point absorbers in advanced ligo. *Applied Optics*, 60(13):4047–4063, 2021.

[Che07] Simon Chelkowski. *Squeezed Light and Laser Interferometric Gravitational Wave Detectors.* PhD thesis, Gottfried Wilhelm Leibniz Universität Hannover, 2007.

[Coh95] Leon Cohen. *Time-frequency analysis*, volume 778. Prentice hall New Jersey, 1995.

[CVDS07] Simon Chelkowski, Henning Vahlbruch, Karsten Danzmann, and Roman Schnabel. Coherent control of broadband vacuum squeezing. *Physical Review A*, 75(4):043814, 2007.

[DDJK15] Rafal Demkowicz-Dobrzański, Marcin Jarzyna, and Jan Kołodyński. Quantum limits in optical interferometry. *Progress in Optics*, 60:345–435, 2015.

[DFGSS21] Christian Darsow-Fromm, Julian Gurs, Roman Schnabel, and Sebastian Steinlechner. Squeezed light at 2128 nm for future gravitational-wave observatories. *Optics Letters*, 46(23):5850–5853, 2021.

[ERB80] J Merle Elson, J Pl Rahn, and Jean M Bennett. Light scattering from multilayer optics: comparison of theory and experiment. *Applied Optics*, 19(5):669–679, 1980.

[EW10] Peter Eaton and Paul West. *Atomic force microscopy.* Oxford university press, 2010.

[FWS$^+$93] M. J. Freeman, H. Wang, D. G. Steel, R. Craig, and D. R. Scifres. Wavelength-tunable amplitude-squeezed light from a room-temperature quantum-well laser. *Opt. Lett.*, 18(24):2141–2143, Dec 1993.

[GDD$^+$13] Hartmut Grote, K Danzmann, KL Dooley, R Schnabel, J Slutsky, and H Vahlbruch. First long-term application of squeezed states of light in a gravitational-wave observatory. *Physical review letters*, 110(18):181101, 2013.

[GHD$^+$15] Tobias Gehring, Vitus Händchen, Jörg Duhme, Fabian Furrer, Torsten Franz, Christoph Pacher, Reinhard F Werner, and Roman Schnabel. Implementation of continuous-variable quantum key distribution with composable and one-sided-device-independent security against coherent attacks. *Nature communications*, 6(1):8795, 2015.

[GK05] Christopher C Gerry and Peter L Knight. *Introductory Quantum Optics.* Cambridge University Press, 2005.

[Hag19] Malte Hagemann. Squeezed-light source at a wavelength of 1550 nm with monolithic cavities. Master's thesis, Universität Hamburg, 2019.

[Hei27] Werner Heisenberg. Über den anschaulichen inhalt der quantentheoretischen kinematik und mechanik. *Zeitschrift für Physik*, 43(3-4):172–198, 1927.

[HGP$^+$06] Gabriel Hétet, Oliver Gloeckl, KA Pilypas, CC Harb, BC Buchler, HA Bachor, and Ping Koy Lam. Squeezed light for bandwidth-limited atom optics experiments at the rubidium d1 line. *Journal of Physics B: Atomic, Molecular and Optical Physics*, 40(1):221, 2006.

[Huh21] Oke Huhs. Automated control of phase matching and double resonance in laser frequency conversion. Master's thesis, Universität Hamburg, 2021.

[HZSS24] Malte Hagemann, Jascha Zander, Axel Schönbeck, and Roman Schnabel. 10-db squeeze laser tuneable over half a nanometer around 1550 nm. *Opt. Express*, 32(5):7954–7958, Feb 2024.

[JYK$^+$21] Wenxuan Jia, Hiroaki Yamamoto, Kevin Kuns, Anamaria Effler, Matthew Evans, Peter Fritschel, et al. Point absorber limits to future gravitational-wave detectors. *Physical Review Letters*, 127(24):241102, 2021.

[KCL21] Hugo Kerdoncuff, Jesper B. Christensen, and Mikael Lassen. Quantum frequency conversion of vacuum squeezed light to bright tunable blue squeezed light and higher-order spatial modes. *Opt. Express*, 29(19):29828–29840, Sep 2021.

[Kha11] Alexander Khalaidovski. *Beyond the Quantum Limit - A Squeezed-Light Laser in GEO 600*. PhD thesis, Gottfried Wilhelm Leibniz Universität Hannover, 2011.

[KPFM93] P Kürz, R Paschotta, K Fiedler, and J Mlynek. Bright squeezed light by second-harmonic generation in a monolithic resonator. *Europhysics Letters*, 24(6):449, 1993.

[KTY$^+$20] Takahiro Kashiwazaki, Naoto Takanashi, Taichi Yamashima, Takushi Kazama, Koji Enbutsu, Ryoichi Kasahara, Takeshi Umeki, and Akira Furusawa. Continuous-wave 6-db-squeezed light with 2.5-thz-bandwidth from single-mode ppln waveguide. *APL Photonics*, 5(3), 2020.

[KVL$^+$12] Alexander Khalaidovski, Henning Vahlbruch, Nico Lastzka, Christian Gräf, Karsten Danzmann, Hartmut Grote, and Roman Schnabel. Long-term stable squeezed vacuum state of light for gravitational wave detectors. *Classical and quantum gravity*, 29(7):075001, 2012.

[LS07] Nico Lastzka and Roman Schnabel. The gouy phase shift in nonlinear interactions of waves. *Optics Express 15*, 7211, 2007.

[MAE$^+$11] Moritz Mehmet, Stefan Ast, Tobias Eberle, Sebastian Steinlechner, Henning Vahlbruch, and Roman Schnabel. Squeezed light at 1550 nm with a quantum noise reduction of 12.3 db. *Optics express*, 19(25):25763–25772, 2011.

[Mal06] Michaela Malec. *Commissioning of advanced, dual-recycled gravitational-wave detectors: simulations of complex optical systems guided by the phasor picture.* PhD thesis, Gottfried Wilhelm Leibniz Universität Hannover, 2006.

[MWV22] Fabian Meylahn, Benno Willke, and Henning Vahlbruch. Squeezed states of light for future gravitational wave detectors at a wavelength of 1550 nm. *Physical Review Letters*, 129(12):121103, 2022.

[PCK92] E S Polzik, J Carri, and H J Kimble. Spectroscopy with Squeezed Light. *Physical Review Letters*, 68:3020–3023, 1992.

[PCL10] Jon Petzing, Jeremy Coupland, and Richard K Leach. The measurement of rough surface topography using coherence scanning interferometry. Measurement good practice guide, December 2010.

[Sch17] Roman Schnabel. Squeezed states of light and their applications in laser interferometers. *Physics Reports*, 684, 2017.

[Sch18] Axel Schönbeck. *Compact squeezed-light source at 1550 nm.* PhD thesis, Universität Hamburg, 2018.

[SHY$^+$85] R E Slusher, L W Hollberg, B Yurke, J C Mertz, and J F Valley. Observation of squeezed states generated by four-wave mixing in an optical cavity. *Physical review letters*, 55(22):2409, 1985.

[SMLC$^+$12] MS Stefszky, CM Mow-Lowry, SSY Chua, DA Shaddock, BC Buchler, H Vahlbruch, A Khalaidovski, R Schnabel, Pa K Lam, and DE McClelland. Balanced homodyne detection of optical quantum states at audio-band frequencies and below. *Classical and Quantum Gravity*, 29(14):145015, 2012.

[Ste13] Sebastian Steinlechner. *Quantum metrology with squeezed and entangled light for the detection of gravitational waves.* PhD thesis, Gottfried Wilhelm Leibniz Universität Hannover, 2013.

[Swi62] Donald F Swinehart. The beer-lambert law. *Journal of chemical education*, 39(7):333, 1962.

[Tea20] ET Steering Commottee Editorial Team. Design report update 2020 for the einstein telescope. Design report, September 2020.

[TJD$^+$13] Michael A Taylor, Jiri Janousek, Vincent Daria, Joachim Knittel, Boris Hage, Hans-A Bachor, and Warwick P Bowen. Biological measurement beyond the quantum limit. *Nature Photonics*, 7(3):229–233, 2013.

[TYK$^+$19] Maggie Tse, Haocun Yu, Nutsinee Kijbunchoo, A Fernandez-Galiana, P Dupej, L Barsotti, CD Blair, DD Brown, SE Dwyer, A Effler, et al. Quantum-enhanced advanced ligo detectors in the era of gravitational-wave astronomy. *Physical Review Letters*, 123(23):231107, 2019.

[Vah08] Henning Vahlbruch. *Squeezed Light for Gravitational Wave Astronomy.* PhD thesis, Gottfried Wilhelm Leibniz Universität Hannover, 2008.

[VCDS07] Henning Vahlbruch, Simon Chelkowski, Karsten Danzmann, and Roman Schnabel. Quantum engineering of squeezed states for quantum communication and metrology. *New Journal of Physics*, 9(10):371, 2007.

[VKL$^+$10] Henning Vahlbruch, Alexander Khalaidovski, Nico Lastzka, Christian Gräf, Karsten Danzmann, and Roman Schnabel. The geo 600 squeezed light source. *Classical and Quantum Gravity*, 27(8):084027, 2010.

[VMC$^+$08] Henning Vahlbruch, Moritz Mehmet, Simon Chelkowski, Boris Hage, Alexander Franzen, Nico Lastzka, Stefan Gossler, Karsten Danzmann, and Roman Schnabel. Observation of squeezed light with 10-db quantum-noise reduction. *Physical review letters*, 100(3):033602, 2008.

[VMDS16] Henning Vahlbruch, Moritz Mehmet, Karsten Danzmann, and Roman Schnabel. Detection of 15 db squeezed states of light and their application for the absolute calibration of photoelectric quantum efficiency. *Physical review letters*, 117(11):110801, 2016.

[Wad16] Andrew Wade. *Quantum Limited Measurements in Gravitational Wave Detectors*. PhD thesis, The Australian National University, 2016.

[WDRS91] Walter Winkler, Karsten Danzmann, Albrecht Rüdiger, and Roland Schilling. Heating by optical absorption and the performance of interferometric gravitational-wave detectors. *Physical Review A*, 44(11):7022, 1991.

[WKHW86] Ling-An Wu, HJ Kimble, JL Hall, and Huifa Wu. Generation of squeezed states by parametric down conversion. *Physical review letters*, 57(20):2520, 1986.

[YNF10] Hidehiro Yonezawa, Koyo Nagashima, and Akira Furusawa. Generation of squeezed light with a monolithic optical parametric oscillator: Simultaneous achievement of phase matching and cavity resonance by temperature control. *Opt. Express*, 18(19):20143–20150, Sep 2010.

[ZM18] Joanna A. Zielińska and Morgan W. Mitchell. Atom-resonant squeezed light from a tunable monolithic pprktp parametric amplifier. *Opt. Lett.*, 43(4):643–646, Feb 2018.

# Resources

Following resources were used to create this thesis:
Mode matchings were calculated with *JamMT* written by Nico Lastzka.
The data was evaluated with *Python 3.10* using the *Anaconda Navigator* and sometimes *Excel*. The scripts for the evaluation in Chapter 5 were written by my former master student Leif Albers. For the Simulation of cavity resonances, the *double resonance calculator* written by Maik Schröder was used.
Technical models and drawings for custom made mechanical components were designed with several versions of *Autodesk Inventor* from 2020 - 2024.
Schematics were done with *Inkscape* and the component library done by Alexander Franzen and Jan Südbeck.
This thesis was written using *Miktex Console 4.9* and *Texmaker 5.0.4*.
Electronic designs for the electronic components existed in the *Non-linear quantum optics* group or were based on them developed by Jan Südbeck, Jascha Zander, Axel Schönbeck.
*Confluence* and *GitLab* were used for documentation.

# Danksagung

I would like to express my gratitude to Roman Schnabel for the opportunity to work this topic and his support, guidance, and feedback throughout the entire process of researching and writing this thesis. His expertise and encouragement have been instrumental in shaping the direction of this work.

I want to acknowledge and thank all the people I worked with during my PhD studies. The support in the lab work and fruitful discussion where a tremendous help and not to mentioned the fun times. I extend my thanks to my family and friends for their support and encouragement during the demanding periods throughout the years. Their encouragement provided the emotional strength needed to navigate the challenges of this academic endeavour.

Lastly, I want to acknowledge the countless individuals who participated in interviews, surveys, or any other form of data collection for this thesis. Your contributions have enriched this study and added depth to its findings.

This thesis would not have been possible without of all those mentioned above. Thank you for being an integral part of this academic journey.

# Eidesstattliche Versicherung

Hiermit versichere ich an Eides statt, die vorliegende Dissertationsschrift selbst verfasst und keine anderen als die angegebenen Hilfsmittel und Quellen benutzt zu haben. Die Dissertation wurde in der vorgelegten oder einer ähnlichen Form nicht schon einmal in einem früheren Promotionsverfahren angenommen oder als ungenügend beurteilt.

Die eingereichte schriftliche Fassung entspricht der auf dem elektronischen Speichermedium.

Ort Datum Unterschrift